The Astrophysical Journal, 874:8 (21pp), 2019 March 20 https://doi.org/10.3847/1538-4357/ab05e2

Changing-look Quasar Candidates: First Results from Follow-up Spectroscopy of Highly Optically Variable Quasars

Chelsea L. MacLeod[1], Paul J. Green[1], Scott F. Anderson[2], Alastair Bruce[3], Michael Eracleous[4], Matthew Graham[5], David Homan[3], Andy Lawrence[3], Amy LeBleu[6], Nicholas P. Ross[3], John J. Ruan[7], Jessie Runnoe[8], Daniel Stern[9], William Burgett[10], Kenneth C. Chambers[11], Nick Kaiser[12], Eugene Magnier[11], and Nigel Metcalfe[13]
[1] Harvard Smithsonian Center for Astrophysics, 60 Garden Street, Cambridge, MA 02138, USA; cmacleod@cfa.harvard.edu
[2] Department of Astronomy, University of Washington, Box 351580, Seattle, WA 98195, USA
[3] Institute for Astronomy, Royal Observatory, Blackford Hill, Edinburgh, UK
[4] Department of Astronomy & Astrophysics and Institute for Gravitation and the Cosmos, 525 Davey Laboratory, The Pennsylvania State University, University Park, PA 16802, USA
[5] Cahill Center for Astronomy and Astrophysics, California Institute of Technology, 1216 E. California Boulevard, Pasadena, CA 91125, USA
[6] Department of Physics, University of Central Florida, 4111 Libra Drive, Orlando, FL 32816, USA
[7] Department of Physics, McGill University, 3600 University Street, Montreal, QC H3A 2T8, Canada
[8] Department of Astronomy, University of Michigan, 1085 S. University Avenue, Ann Arbor, MI 48109, USA
[9] Jet Propulsion Laboratory, California Institute of Technology, 4800 Oak Grove Drive, Mail Stop 169-221, Pasadena, CA 91109, USA
[10] GMTO Corp., 251 S. Lake Avenue, Pasadena, CA 91101, USA
[11] Institute for Astronomy, University of Hawaii at Manoa, Honolulu, HI 96822, USA
[12] Ecole Normale Supérieure ENS, 24, rue Lhomond, Paris, F-75005, France
[13] Department of Physics, University of Durham Science Laboratories, South Road, Durham DH1 3LE, UK
Received 2018 September 28; revised 2019 January 22; accepted 2019 February 6; published 2019 March 15

Abstract

Active galactic nuclei (AGNs) that show strong rest-frame optical/UV variability in their blue continuum and broad line emission are classified as changing-look AGN, or at higher luminosities, changing-look quasars (CLQs). These surprisingly large and sometimes rapid transitions challenge accepted models of quasar physics and duty cycles, offer several new avenues for study of quasar host galaxies, and open a wider interpretation of the cause of differences between broad and narrow-line AGN. To better characterize extreme quasar variability, we present follow-up spectroscopy as part of a comprehensive search for CLQs across the full Sloan Digital Sky Survey (SDSS) footprint using spectroscopically confirmed quasars from the SDSS DR7 catalog. Our primary selection requires large-amplitude ($|\Delta g| > 1$ mag, $|\Delta r| > 0.5$ mag) variability over any of the available time baselines probed by the SDSS and Pan-STARRS 1 surveys. We employ photometry from the Catalina Sky Survey to verify variability behavior in CLQ candidates where available, and confirm CLQs using optical spectroscopy from the William Herschel, MMT, Magellan, and Palomar telescopes. For our adopted signal-to-noise ratio threshold on variability of broad Hβ emission, we find 17 new CLQs, yielding a confirmation rate of $\gtrsim$20%. These candidates are at lower Eddington ratio relative to the overall quasar population, which supports a disk-wind model for the broad line region. Based on our sample, the CLQ fraction increases from 10% to roughly half as the continuum flux ratio between repeat spectra at 3420 Å increases from 1.5 to 6. We release a catalog of more than 200 highly variable candidates to facilitate future CLQ searches.

Key words: accretion, accretion disks – catalogs – quasars: emission lines

Supporting material: machine-readable tables

1. Introduction

Quasars are known to vary on the 10% to 20% level over time (∼months–years) and across many wavelengths. Their continuum variability is intrinsic to the central engine, and it causes a response in the broad emission line (BEL) flux that is usually lagged and has a smaller amplitude (Peterson et al. 2004; Bentz et al. 2009). Extreme variations in optical continuum/BEL flux, besides enabling robust studies of the response between various emission components, have been caught in recent surveys of the sky (e.g., Stern et al. 2017; Assef et al. 2018) and can reveal rare, interesting physics. There are various scenarios for the underlying accretion disk structure that could explain strong rapid variability in active galactic nucleus (AGN). These include magnetically elevated (or "thick") disks (Dexter & Begelman 2019), accretion state transitions (Noda & Done 2018), instabilities arising from magnetic torque near the inner stable circular orbit of the accretion disk (Ross et al. 2018), and misaligned disks Nixon et al. (2012).

Besides variability, quasar spectra yield information on the structure of the emission regions. The Balmer lines are thought to provide the most direct measurement of the amount of ionizing flux relative to the other BELs, and the Hβ BEL is classically used, along with Hα, to define AGN types (Osterbrock 1981). The profiles of higher ionization lines seen in the UV (C IV$\lambda\lambda$1548,1550, C III]λ1909) often reveal powerful outflows (Richards et al. 2011). The Mg IIλ2800 line is generally less responsive to changes in ionizing flux than the Balmer lines, presumably due to a larger average formation radius and/or because it is intrinsically less responsive (Korista & Goad 2004), but in recent analysis the line has been observed to reverberate among SDSS-RM quasars similarly to Hβ (Shen et al. 2016). In the disk-wind model for the BLR described by Elitzur et al. (2014), the dividing line between a Type 1 and "true" (unobscured) narrow-line Type 2 AGN is a critical value of a parameter: $L/M_{\rm BH}^{2/3}$, similar to the Eddington ratio. Conversely, obscured Type 2 quasars can mostly be explained

Table 1
Selection of Spectroscopically Variable Quasars

Selection	Total #	$i_{SDSS} < 19.5$/ Has CRTS	Extended Morphology	*Chandra*/ *XMM*
SDSS Quasars in DR7Q	105783	69420	4392	⋯
Lacking BOSS spectra	79838	53594	4142	⋯
EVQs: $\|\Delta g\| > 1$ mag, $\|\Delta r\| > 0.5$ mag ($\sigma < 0.15$ mag), $z < 0.83$	1727	1081	416	⋯
Lacking radio detection	1403	858	332	103
$\|\Delta g\| > 1$ mag as of 2013	262	203	86	20
Observed spectroscopically (MMT: 64%, Mag.: 15%, WHT: 15%, Pal.: 6%)	130	105	67	17
CLQs: Hβ (dis)appearance at N_σ(Hβ) > 3	17	15	10	0

Note. Each step includes the criteria listed on the previous rows. The rightmost three columns describe prioritized subsets that do not together comprise the full sample in the leftmost column. Our X-ray catalog is limited to radio-quiet objects.

by varying orientation, as can obscured Type 1 AGN (Liu et al. 2018).

A small fraction of AGN show large changes in Balmer BELs and are called "changing-look" AGN (CLAGN) if over time they significantly lose or gain BEL flux (Khachikian & Weedman 1971; Tohline & Osterbrock 1976; Penston & Perez 1984; Cohen et al. 1986; Goodrich 1989; Storchi-Bergmann et al. 1993; Bischoff & Kollatschny 1999; Eracleous & Halpern 2001; Denney et al. 2014; Shappee et al. 2014; Li et al. 2015; Husemann et al. 2016; Runco et al. 2016). These optical CLAGN are different from the classical CLAGN discovered in the X-rays (Risaliti et al. 2009), which are generally associated with large changes in the X-ray absorption column. Changing-look quasars (CLQs) have recently been defined as AGN with a bolometric luminosity $L_{bol} > 10^{44}$ erg s^{-1} that exhibit a strong change in Balmer BELs, usually changing between Types 1 and 1.9 in the optical, and have been recently discovered in surveys featuring large sample size and long time baselines (LaMassa et al. 2015; MacLeod et al. 2016; Ruan et al. 2016; Runnoe et al. 2016; Gezari et al. 2017; Stern et al. 2018; Yang et al. 2018). Presumably, CLQs are due to the same phenomena as optical CLAGN, but at higher luminosity and redshift. In the handful of cases where there exists X-ray coverage before and after the event, there are no signs of associated changes in absorption (e.g., LaMassa et al. 2015), therefore suggesting that strong intrinsic changes in the central ionizing flux are responsible.

In MacLeod et al. (2016), we performed a systematic search for CLQs through archival spectra in the Sloan Digital Sky Survey (SDSS) among quasars with repeat spectra. This method takes advantage of full-sky photometric surveys to select a sample of strongly variable quasars. Now, we use follow-up spectroscopy to uncover additional CLQs. Recently, Rumbaugh et al. (2018) showed that extremely variable quasars (EVQs, defined as having $\Delta g > 1$ mag over any baseline) account for 30%–50% of quasars, and they are systematically at lower Eddington ratio than their less variable counterparts. The authors only implied that by extension, CLQs follow this trend. We are now able to specifically confirm this trend with our follow-up spectroscopy. We also determine what fraction of highly variable quasars show strong BEL changes as a function of continuum flux change using spectral decomposition.

We outline the input photometric data and CLQ candidate selection in Section 2 and the spectroscopic data and analysis in Section 3. We present our results from spectroscopic follow-up of CLQ candidates, including the sample demographics and CLQ fraction in Section 4. Since the purpose of this work is to systematically search for physically interesting or rare events that might shed light on the structure in and around accretion disks, we only highlight the most significant and dramatic cases. However, we provide the full candidate sample since it may be used for studying the highly variable tail of quasar variability. The results are summarized and discussed in Section 5.

2. Photometry and Analysis

We use imaging data from the SDSS and Pan-STARRS 1 (PS1; Kaiser et al. 2002) to select strongly variable quasars for spectroscopic follow-up. In this section, we describe the input data and our sample selection (see Table 1 for a summary).

2.1. Optical Photometry

2.1.1. SDSS

The SDSS (York et al. 2000) uses the imaging data gathered by a dedicated 2.5 m wide-field telescope (Gunn et al. 2006), which collected light from a camera with 30 2k × 2k CCDs (Gunn et al. 1998) over five broad bands—*ugriz* (Fukugita et al. 1996)—to image 14,555 unique deg^2 of the sky. This area includes 7500 deg^2 in the North Galactic Cap (NGC) and 3100 deg^2 in the South Galactic Cap (SGC). SDSS started its imaging campaign in 2000 and concluded in 2007, having covered 11,663 deg^2. These data are part of the SDSS I/II survey and are described in Abazajian et al. (2009) and references therein. SDSS-III added another ∼3000 deg^2 of new imaging area in 2008.

The imaging data are taken on dark photometric nights of good seeing (Hogg et al. 2001), calibrated photometrically (Smith et al. 2002; Ivezić et al. 2004; Tucker et al. 2006; Padmanabhan et al. 2008), and astrometrically (Pier et al. 2003) before object parameters are measured (Lupton et al. 2001; Stoughton et al. 2002). The Eighth Data Release (DR8; Aihara et al. 2011) provides updated photometric calibrations.

The Stripe 82 region of SDSS (S82; $22^h24^m <$ R.A. $< 04^h08^m$ and $|$ decl.$| < 1.^\circ27$) covers ∼300 deg^2 and has been observed ∼60 times on average to search for transient, variable, and moving objects (Abazajian et al. 2009). These multi-epoch data have timescales ranging from 3 hr to 8 yr and provide well-sampled five-band light curves for an unprecedented number of quasars.

In our variability analysis and determination of the source morphology,[14] we include all DR10 primary and secondary

[14] If any epoch has a point-source morphology in SDSS, the object is considered a point source.

photometry, as well as observations for point sources in Stripe 82 taken in nonphotometric conditions and recalibrated using the improved method of Ivezić et al. (2004).

2.1.2. Pan-STARRS 1 3π

Our analysis includes imaging from the PS1 3π survey, in particular the Processing Version 2 catalog available in a local Desktop Virtual Observatory (DVO) database (released 2015 January). The overall survey is described in Chambers et al. (2016); see Magnier et al. (2016a, 2016b, 2016c), Waters et al. (2016), and Flewelling et al. (2016) for a description of the data analysis and products. PS1 observations were made with a 1.8 m telescope equipped with a 1.4 gigapixel camera. Over the course of 4 yr of the 3π survey, up to four exposures per year in five bands, $g_{\rm P1}$, $r_{\rm P1}$, $i_{\rm P1}$, $z_{\rm P1}$, $y_{\rm P1}$, have been taken across the full $\delta > -30^\circ$ sky. Each nightly observation consists of a pair of exposures 15 min apart to search for moving objects. For each exposure, the PS1 3π survey has a typical 5σ depth of 22.0 in the *g*-band (Inserra et al. 2013). Pan-STARRS imaging commenced in 2009 and continued through to 2013. Hence, the addition of the PS1 photometry to the SDSS photometry increases the baseline of observations from ≈8 to ≈14 yr with typically several epochs over the overlapping area between the SDSS and (∼30,000 deg^2) PS1 footprints.

2.1.3. Catalina Sky Survey

The Catalina Real-time Transient Survey (CRTS) is an open-band large-scale survey with dense monitoring by multiple telescopes of sources brighter than $i \lesssim 19.5$. See Drake et al. (2009) for details. The CRTS magnitudes are calibrated to a *V*-band zero-point. Where available, CRTS light curves add the most recent monitoring data (up to 2016), and the largest number of imaging epochs (typically ∼300 over 10 yr). The data displayed are averaged in 10 day segments.

2.2. Radio Detections

To exclude potential jet-related variability from our sample of light curves, we match to the unified radio catalog of Kimball & Ivezić (2014) using a 30″ matching radius. This includes data from the FIRST, NVSS, WENSS, GB6 radio surveys, as well as VLA Low-frequency Sky Survey revised edition (VLSSr).

2.3. CLQ Candidate Selection

We use optical photometric variability from SDSS and PS1 to select quasars for follow-up optical spectroscopy. This is a similar selection as in MacLeod et al. (2016), which was based on $\Delta g > 1$mag changes among SDSS/PS1 photometry and repeat spectra in SDSS and the SDSS-III's Baryon Oscillation Spectroscopic Survey (BOSS; Dawson et al. 2013). To extend our previous work, we follow up highly variable quasars lacking recent spectra in BOSS. For selecting targets, we limit the sample to redshifts $z < 0.83$ so that the Hβ line is within the optical wavelength range.

In particular, CLQ candidates are selected by requiring (i) a magnitude change of $\Delta g > 1$ mag and $\Delta r > 0.5$ mag among SDSS and PS1 measurements with errors <0.15 mag, (ii) no radio detection to exclude jet-related variability, (iii) a redshift $z < 0.83$, (iv) no BOSS spectrum, and (v) a current *g* magnitude at least 1 mag dimmer or brighter compared to the SDSS spectral epoch. For (v), the photometric data point nearest in time to the earliest SDSS spectrum is compared to the most recent PS1 data point. After visual vetting of the combined SDSS/PS1/CRTS light curves and spectra, we arrive at 262 CLQ candidates, listed in Table 2. Table 1 summarizes each stage of filtering. We prioritize these candidates based on a number of factors to most efficiently use telescope time. These include their morphology to minimize overlap with the sample from the Time Domain Spectroscopy Survey (TDSS) "HYPQSO" program, which is obtaining few-epoch-spectroscopy for hypervariable quasars (Morganson et al. 2015; MacLeod et al. 2018), but only those with point-source morphology in SDSS; X-ray detections from the second release of the *Chandra* Source Catalog (CSC; Evans et al. 2018) and/or the *XMM-Newton* 3XMM-DR5 (Rosen et al. 2016) catalog, since they afford the opportunity for follow-up with X-ray observatories; the signal-to-noise ratio (S/N) in the earlier spectrum; and the most recent photometry from CRTS. While there is no straightforward algorithm to select the 130 observed targets out of the 262 candidates, Table 1 gives the breakdown into three main criteria for prioritization in the last three columns, for each stage of filtering.

3. Spectroscopy and Analysis

Starting with a spectroscopic quasar catalog from SDSS, we target highly variable quasars for new optical spectroscopy. We describe the SDSS and follow-up spectroscopic data sets in Section 3.1, and describe our spectral analysis in Section 3.2. A complete log of the spectroscopic observations and other relevant information can be found in Table 2.

3.1. Spectroscopic Data

3.1.1. SDSS/BOSS

The final spectroscopically confirmed quasar catalog from SDSS I/II, based on the Seventh Data Release of SDSS (DR7; Abazajian et al. 2009), is presented in Schneider et al. (2010). This catalog contains 105,783 quasars that have luminosities larger than $M_i = -22.0$. These quasars form our parent sample, and are hereafter referred to as the *DR7Q catalog*.

As described by Richards et al. (2002), the bulk of quasar target candidates in SDSS I/II were selected for spectroscopic observations based on their optical colors and magnitudes in the SDSS imaging data or their detection in the FIRST radio survey (Becker et al. 1995). Low-redshift, $z \lesssim 3$, quasar targets were selected based on their location in *ugri*-color space, and the quasar candidates passing the *ugri*-color selection are selected to a flux limit of $i = 19.1$. High-redshift, $z \gtrsim 3$, objects were selected in *griz*-color space and are targeted to $i = 20.2$. Furthermore, if an unresolved, $i \leqslant 19.1$ SDSS object is matched to within 2″ of a source in the FIRST catalog, it is included in the quasar selection. Additional quasars were also (inhomogeneously) discovered and cataloged in SDSS I/II using X-ray, radio, and/or alternate odd-color information, and extending to fiber-magnitudes of about $m < 20.5$ (e.g., see Anderson et al. 2003).

In MacLeod et al. (2016), we looked for significant changes in the BELs of quasars that had a second epoch of spectroscopy in BOSS, which was part of the third incarnation of the SDSS (SDSS-III; Eisenstein et al. 2011). In this work, we target quasars that lack a BOSS (DR12) spectrum, with two

Table 2
CLQ Candidates

SDSSJID	z	morph. flag	Phot. MJD_1	g_1 (mag)	σ_1 (mag)	Phot. MJD_2	g_2 (mag)	σ_2 (mag)	Spec. MJD_1	MJD (PS1)	g_{PS1} (mag)	σ_{PS1} (mag)	Spec. MJD_2	Facility	CLQ by VI?	N_σ (Hβ)
000116.00+141123.0	0.404	0	52170	18.696	0.021	56588	21.009	0.071	52235	56588	21.009	0.071	57989	MMT	0	2.6
000904.54−103428.7	0.241	0	51814	17.795	0.028	55860	19.123	0.022	52141	55860	19.123	0.022	58367	MMT	1	8.2
001113.46−110023.5	0.495	1	51865	19.885	0.031	55829	21.308	0.112	52141	55834	21.233	0.113	57989	MMT	1	2.3
001206.25−094536.3	0.566	0	51865	19.061	0.049	56218	21.638	0.148	52141	56218	21.638	0.148	57597	Magellan	1	2.5
001502.38−094439.1	0.336	1	51865	18.877	0.022	56214	20.349	0.073	52138	56218	20.283	0.055	57595	Magellan	0	2.0
002311.06+003517.5	0.422	0	51081	19.584	0.024	55449	18.079	0.032	55480	56206	18.728	0.016	58037	MMT	1	2.4
002450.50+003447.7	0.524	1	52522	18.766	0.030	55449	19.921	0.133	52203	56206	19.814	0.029	57989	MMT	0	0.4
002627.89−101020.5	0.718	0	51814	19.534	0.026	55829	20.611	0.066	52145	55829	20.583	0.063	57596	Magellan	0	0.7
002714.21+001203.7	0.454	0	51081	18.261	0.007	56206	19.466	0.024	51782	56206	19.466	0.024	57726	MMT	0	2.0
004339.32+134436.5	0.527	0	51464	19.349	0.022	55499	21.997	0.146	51879	55829	21.248	0.104	57597	Magellan	1	3.1
005244.14+142807.1	0.652	0	51464	19.254	0.021	55745	20.478	0.034	51871	55745	20.478	0.034	57597	Magellan	0	0.7
012821.43+151956.4	0.548	0	51464	18.669	0.039	55810	20.190	0.032	51893	55810	20.190	0.032	57597	Magellan	0	2.2
012946.71+150457.2	0.365	0	51465	17.700	0.023	55835	20.474	0.098	51898	56246	20.029	0.101	57597	Magellan	0	5.9
013203.46−093153.6	0.190	1	51814	18.439	0.025	56209	19.479	0.024	52178	56209	19.479	0.024	57726	MMT	0	5.7
013458.36−091435.4	0.443	0	51814	18.605	0.022	56209	19.985	0.036	52178	56209	19.970	0.035	57989	MMT	1	5.5
015957.64+003310.4	0.312	1	51819	19.122	0.026	54424	20.284	0.049	51871	55863	19.942	0.044	55201	BOSS	1	–
022556.07+003026.7	0.504	1	52522	19.974	0.029	55508	21.783	0.134	52944	56214	20.710	0.178	55445	BOSS	1	–
022652.24−003916.5	0.625	0	52288	20.252	0.023	55932	22.002	0.089	52641	56214	21.676	0.186	56577	BOSS	1	–
025428.83−004834.9	0.810	0	52585	19.759	0.027	56214	20.831	0.087	52614	56214	20.831	0.087	N/A	N/A	–	–

Note. The full list of 262 candidates are available in the electronic version. Fields are marked with "−" if the repeat spectra were not analyzed (due to either data source or S/N) or not available. The third column lists the morphology flag (0 for point source, 1 if extended).

(This table is available in its entirety in machine-readable form.)

exceptions: two of the CLQs from MacLeod et al. (2016), J002311.06+003517.5 and J225240.37+010958.7, were targeted for follow-up spectroscopy here because they showed a strong dimming in PS1 since the BOSS spectrum.

3.1.2. William Herschel Telescope (WHT)

Relatively bright ($g < 20.5$) and highly variable ($|\Delta g| > 1.3$ mag) CLQ candidates were observed on the nights of 2016 February 6–8 and May 30, 31 using the 4.2 m WHT in La Palma. Observations were performed using the Intermediate dispersion Spectrograph and Imaging System (ISIS). The 5300 dichroic was used along with the R158B and R300B gratings in the red and blue arms, respectively, along with the GG495 order sorting filter in the red arm. Typically 2× binning in the spatial direction was used to improve the S/N, along with a narrow CCD window to reduce memory usage and readout times. This setup gives a spectral resolution of $R \sim 1500$ at 5200 Å in the blue and $R \sim 1000$ at 7200 Å in the red for a slit width of 1.″0 and nominal total coverage of ∼3100 to 10,600 Å (but effectively further limited by the atmosphere).

Typically, calibration images were taken at the start of each night, including bias frames, lamp flats, and CuNe/Ar arc lamp images. Spectroscopic standard stars were observed at ∼2 hr intervals throughout the night, though this cadence was not always possible. The slit was oriented at the parallactic angle. Exposures were taken in 1800 s increments, and the number of shots on target was adjusted based on the latest PS1 photometry. WHT data were reduced using custom PYRAF scripts and standard techniques.

For analysis of follow-up spectra from WHT and other telescopes described as follows, we correct for telluric absorption where needed by using a standard star observation at similar airmass and the empirical method described in Wade & Horne (1988) and Osterbrock et al. (1990).

3.1.3. MMT

Observations of a fainter set of targets were made with the Blue Channel Spectrograph on the 6.5 m MMT situated on Mount Hopkins, Arizona. Observations were carried out over several dates in 2016 to 2018 (see Table 2 for exact dates). Here, the 300 ℓ mm^{-1} grating was used with a clear filter and 2× binning in the spatial direction. The central wavelength setting ranged from 5835 to 6335 Å (mostly at 5900 Å). To reduce MMT data, we used the `pydis` software adapted for use with Blue Channel data.[15] We use three exposures to remove cosmic rays by taking the median, and we compute the error in flux as rms/$\sqrt{N}$. When three exposures were not available, we used the errors output by `pydis` and removed cosmic rays by filtering large deviations from the background regions on the smoothed two-dimensional spectrum. The Blue Channel spectrograph (on MMT) achieves good signal at observed-frame wavelengths $\lambda < 7000$ Å.

3.1.4. Magellan

To observe most of our targets in the SGC, and most of the relatively high-redshift targets, we used the *Magellan* Clay 6.5 m telescope with the Low Dispersion Survey Spectrograph 3 (LDSS3)-C spectrograph. Observations were carried out over the nights 2016 July 26–29. The LDSS3-C instrument consists of a grism situated behind an aperture plate; we opted to use the VPH-All grism (covering 4250–10000 Å) with the standard 1.″0 × 4.′0 center long slit mask.

The LDSS3-C spectrograph has better efficiency toward redder wavelengths ($7000 < \lambda < 10000$ Å) than the MMT's Blue Channel, so we preferred it for higher-redshift objects. Reductions were carried out using both standard IRAF techniques and the `pydis` software adapted for use with LDSS3 data.

3.1.5. Palomar

We obtained second-epoch spectra of two quasars with Double Spectrograph (DBSP) on the Hale 200″ Telescope at Palomar Observatory on UT 2017 May 30, and second-epoch spectra of an additional six quasars using the same instrument on UT 2017 June 26. All quasars were observed with single 900 s exposures, other than J161602.39+482201.2, which was observed with two such exposures. We obtained all the spectra through a 1.″5 slit aligned at the parallactic angle using the 600 ℓ mm^{-1} grating on the blue arm of the spectrograph ($\lambda_{\rm blaze} = 4000$ Å), the 316 ℓ mm^{-1} grating on the red arm of the spectrograph ($\lambda_{\rm blaze} = 7500$ Å), and the 5500 Å dichroic. This configuration provides moderate resolution spectra across the entire optical window. The data were processed using standard techniques within IRAF, and flux calibrated using standard stars observed on the same night.

3.2. Spectral Decomposition

We use the QSfit spectral decomposition code from Calderone et al. (2017) to analyze the SDSS and follow-up spectra. We fit simple power-law continuum components, iron optical and UV templates, Balmer continuum, BEL, narrow emission line, and host galaxy components. The Fe II templates are based on the narrow-line Seyfert 1 (NLS1) AGN I Zw 1 (Vestergaard & Wilkes 2001; Véron-Cetty et al. 2004), with the UV iron equivalent width (EW) fixed to avoid a degeneracy with the continuum slope. The host galaxy template is a typical AGN host (Silva et al. 1998; Polletta et al. 2007). We adopt the redshifts and $E(B-V)$ values from the DR7Q catalog. We exclude spectra where the median S/N is $\lesssim$2. For an example spectral decomposition near Hβ, see Figure 1.

For the Hβ line, we start by fitting a single broad plus a single narrow component with both FWHM values allowed to vary. The FWHM of the broad component was limited to be between 900 and 15,000 km s^{-1}, as in Calderone et al. (2017). The narrow lines were modeled with single components with a FWHM limited to the range 100 to 2000 km s^{-1}. For some objects, the broad Hβ component was flagged as having bad quality (e.g., the FWHM or velocity offset hit a limit). In these cases, if there was no apparent broad Hβ flux (which was usually the case), we fixed the FWHM of the broad component to the full width at 10% maximum of the broad component from the bright-state spectrum to find an upper limit on the Hβ flux.[16]

After fitting each spectrum, we scaled the follow-up spectrum by a single factor so that the modeled sum of narrow [O III]$\lambda\lambda$4959,5007 Å line flux (continuum-subtracted) matched that of the early-epoch SDSS spectrum. In some cases where

[15] http://jradavenport.github.io/2015/04/01/spectra.html

[16] Our results are not affected whether we use the full width at 10% maximum or the FWHM of the bright-state Hβ flux for the CLQ dim-state flux.

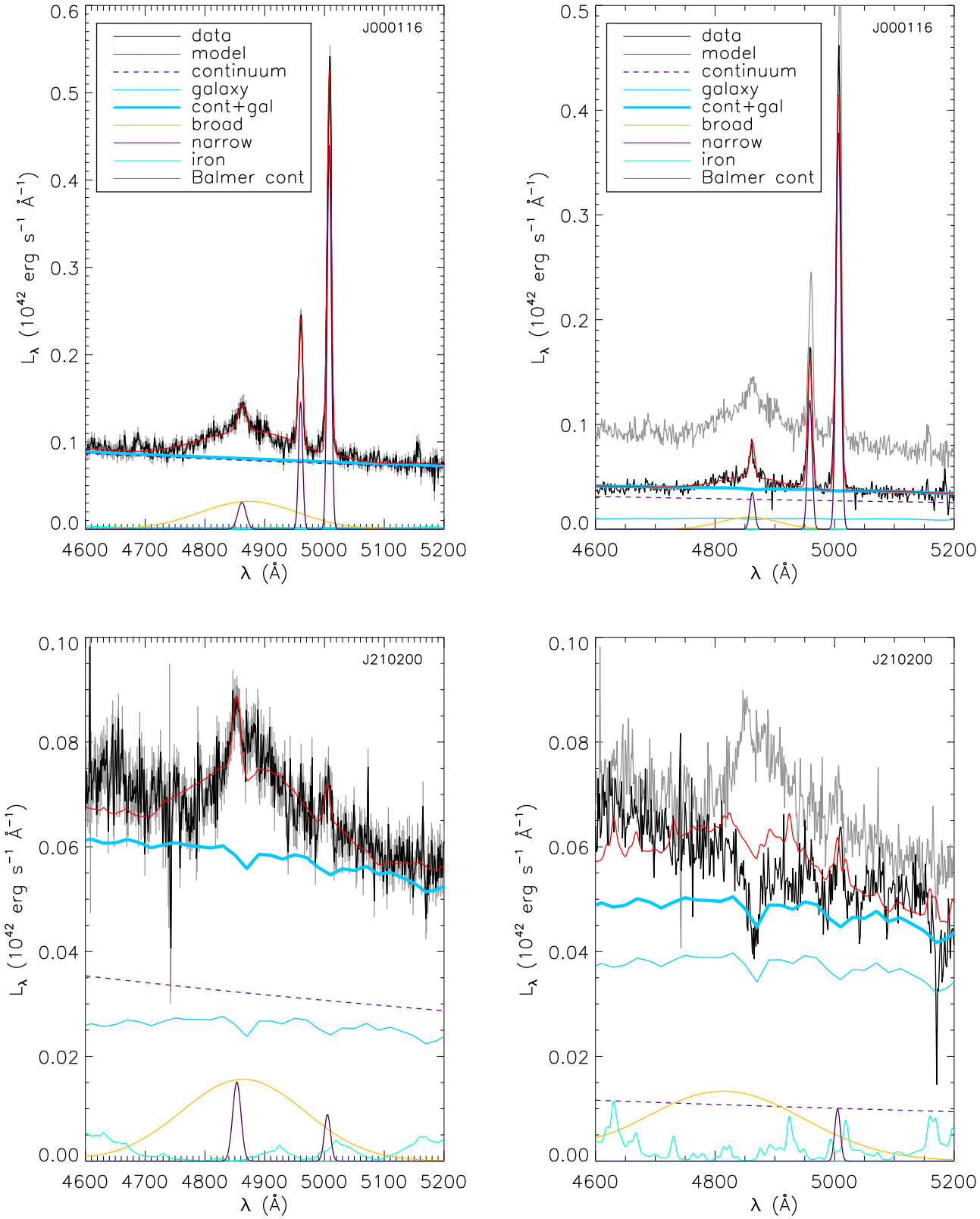

Figure 1. Top panels: example of a spectral decomposition for variable quasar J000116.00+141123.0 showing an intermediate luminosity change ($|\Delta L_{3240}| \simeq 3.5 \times 10^{44}$ erg s^{-1}) and retaining some broad Hβ flux. This object is not classified as a CLQ here because there is still broad Hβ visible in the dim state, and the significance of the BEL change is $N_\sigma(\mathrm{H}\beta) < 3$. In the left panel, the SDSS spectrum, best-fit model, and model components are shown. In the right panel, the SDSS spectrum is shown in gray, and the spectral decomposition for the follow-up spectrum, in black, is shown. The follow-up spectra are scaled so that the integrated [O III]$\lambda\lambda$4959,5007 Å model narrow-line flux matches that of the SDSS spectrum. Bottom panels: as in the top panels but for J210200.42+000501.8, a changing-look quasar in a post-starburst galaxy (Cales et al. 2013). In this case, the BEL component fit to the dimmer spectrum was fixed to 10% the SDSS flux and is considered only an upper limit.

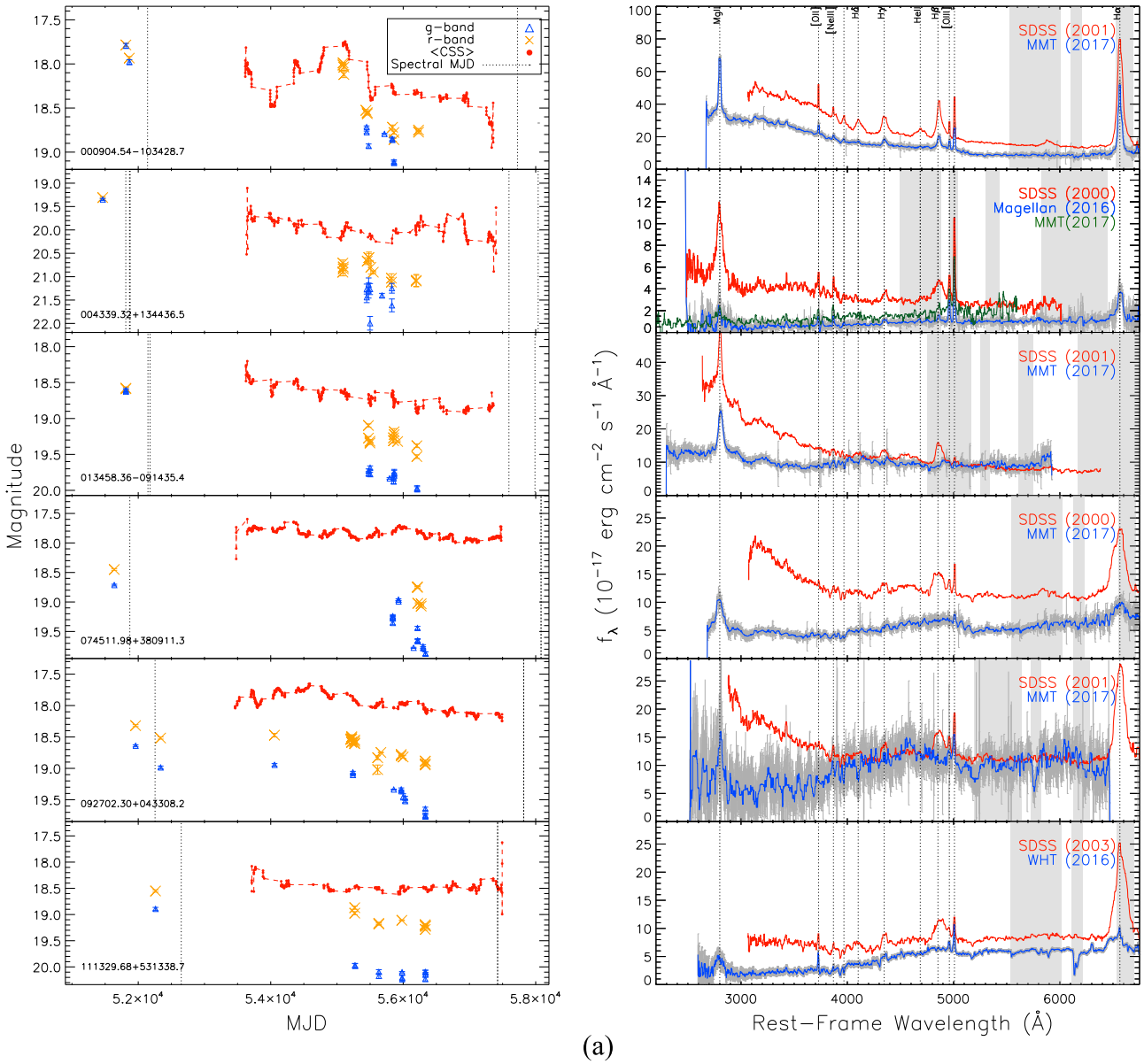

(a)

Figure 2. CLQ light curves and repeat spectra shown in R.A. order. Left: SDSS and Pan-STARRS *g*-band (*r*-band) photometry is shown as blue triangles (orange crosses). Red data points show archival photometry from CRTS in unfiltered light, averaged every 10 days. The existing spectroscopic epochs are indicated by the vertical lines. Right: existing spectra for objects in the adjacent left panel (red is SDSS; blue or green is our follow-up), corrected for telluric absorption where needed. The telluric bands are shown in gray, as are the error bars in flux. The follow-up spectra plotted in green improve the coverage to shorter or longer wavelengths, but are not included in the analysis (their errors are not shown).

the [O III] scaling yielded unphysical results, we instead forced the host galaxy component to match that of SDSS.

Then, using the Monte Carlo resampling technique from Calderone et al. (2017), we resampled 100 times, taking the rms of the resulting parameters for their uncertainties.

3.3. Definition of CLQs

The S/N can have a large impact on the visual definition of CLQs. If the S/N were worse for certain objects (e.g., J000116.00+141123.0 shown in Figure 1), they might be considered CLQs upon visual inspection, as Hβ would be hidden in the noise. To limit the number of cases that simply lacked the S/N to rule out a CLQ nature, we use the significance of the Hβ change to form our CLQ sample.

We calculate the flux deviation,

$$N_\sigma(\lambda) = (f_2 - f_1)\Big/\sqrt{\sigma_2^2 + \sigma_1^2}, \quad (1)$$

to determine the significance (in units of σ per spectral element) for the Hβ change. First, we scale the spectra as described in Section 3.2 and subtract each continuum component to remove the linear trend across the line. Then, we re-bin the spectra to a similar resolution in rest-frame wavelength of about 2 Å/pix. Finally, we smooth the resulting spectra using a running median with a window of 32 Å (rest frame). The most extreme value of $N_\sigma(\lambda)$ in the wavelength range of Hβ (4750–4940 Å rest frame), indicative of the amount of Hβ variability, is then compared to N_σ(4750 Å)—that is, the flux deviation just blueward of Hβ. Note that the value N_σ(4750 Å) is determined from

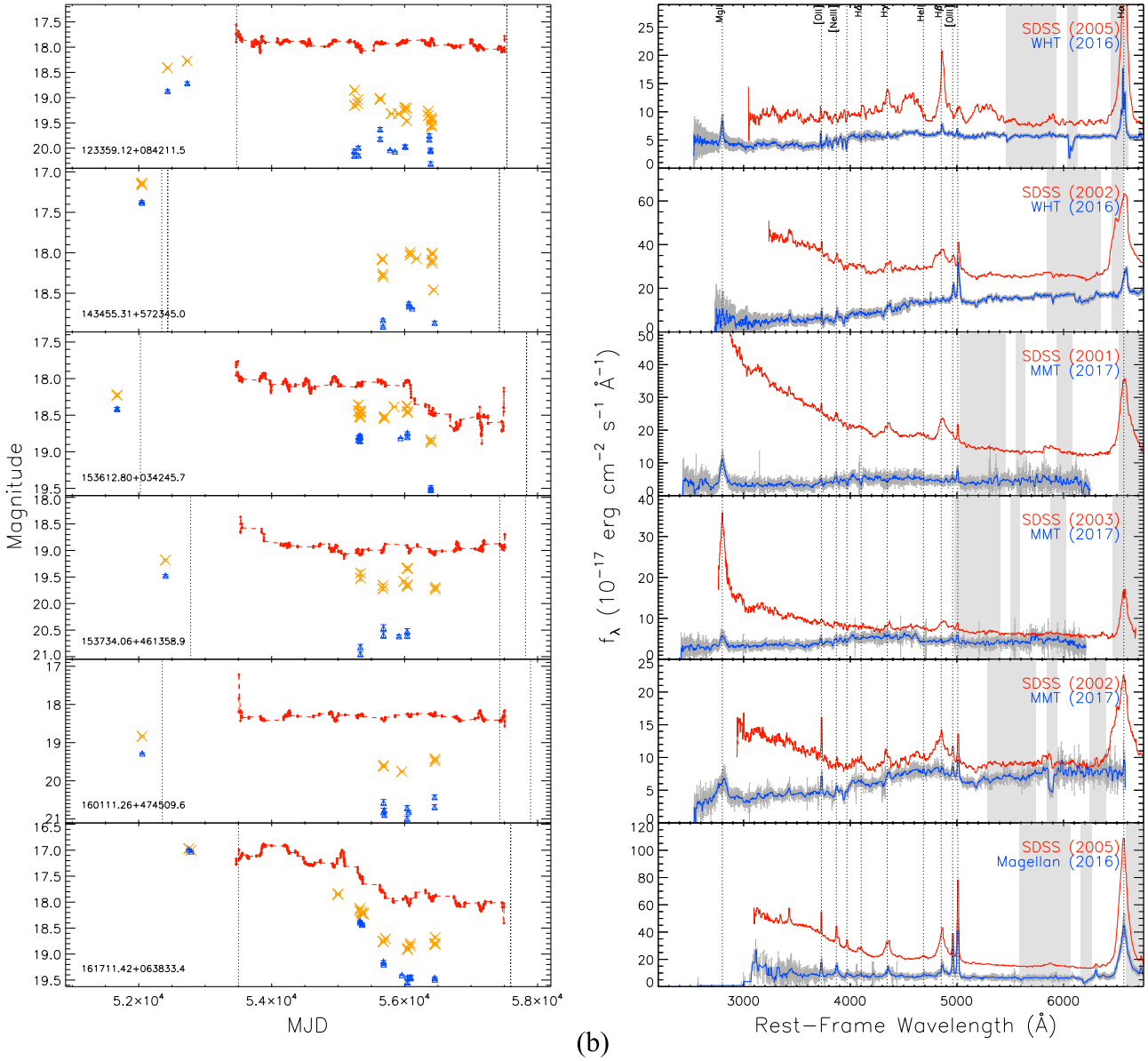

Figure 2. (Continued.)

the smoothed array so that we are not susceptible to outliers in flux at that wavelength. This method is designed to detect Hβ variability relative to the 4750 Å continuum: if the maximum $|N_\sigma(\lambda)|$ of the line exceeds the flux deviation in the neighboring continuum by a certain amount, the object may be classified as a CLQ. We compute the maximum flux deviation of the line relative to the continuum N_σ(4750–4940 Å) − N_σ(4750 Å), which we express as N_σ(Hβ).

We define CLQs as having a visual disappearance (or emergence) of broad Hβ at a $N_\sigma(\mathrm{H}\beta) > 3$ level. In Table 2, the visually identified CLQs are indicated by a "1," and N_σ(Hβ) is also provided. At least half of the apparent "CLQs" from our visual inspection had $N_\sigma(\mathrm{H}\beta) < 3$; these objects would benefit from better quality spectra to confirm or refute the absence of broad BEL components.

We note that by using a N_σ(Hβ) definition, we may identify as CLQs objects whose broad Hβ does not change by a large amount. However, our definition is primarily a practical one, as it uses quantities that we can readily measure. An alternative criterion such as an absolute or relative change in broad Hβ flux would lead to a different set of ambiguities. Moreover, so far CLQs have most often been identified by visual inspection of the spectra without a quantitative definition. Therefore, we adopt this straightforward definition and explore the consequences.

4. Results

Using the WHT, MMT, Magellan, and Palomar, follow-up spectra have been obtained for 130 sources. In Table 2, we list all objects selected as CLQ candidates and indicate those already observed with follow-up spectroscopy. Included in the table are the two g-band photometric measurements leading to the $\Delta g > 1$ mag selection (g_1 and g_2 with associated errors σ_1 and σ_2), along with their MJDs (MJD$_1$ and MJD$_2$). We also list the most recent g-band magnitude (g_{PS1}) and spectral epochs (SDSS and follow-up).

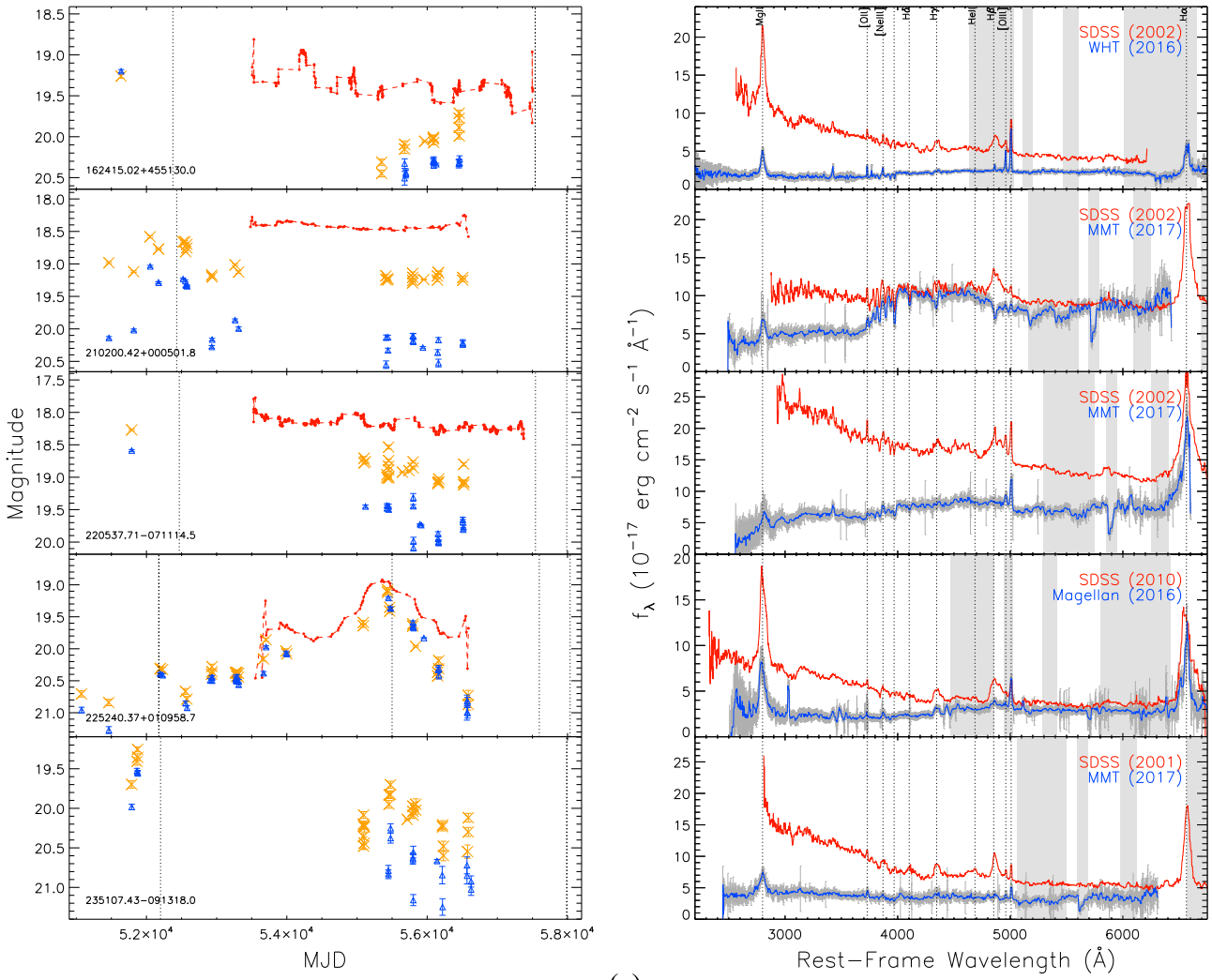

(c)

Figure 2. (Continued.)

The repeat spectra for the highest-confidence CLQs with $N_\sigma(\mathrm{H}\beta) > 3$, numbering at 17, and the corresponding light curves are shown in Figure 2. Lower-confidence CLQs with $1 < N_\sigma(\mathrm{H}\beta) < 3$ are shown in the Appendix (Figure 7). The light curves suggest a strong dimming (or brightening) between the spectral epochs, but in most cases there is not enough photometric sampling to resolve the timescale for the change. The CRTS data resolve the time of transition more often than the SDSS/PS1 light curves, but due to the unfiltered bandpass, the CRTS light curves are less sensitive than the *g*-band to blue continuum variability. The results from light curve modeling (following Kozłowski et al. 2010; MacLeod et al. 2010) and characterization (following Kim et al. 2011) of the SDSS/PS1 or CRTS photometry essentially confirm our selection of CLQ candidates: that they have a large change in flux at some point between the SDSS and Pan-STARRS data (leading to longer characteristic timescales). Among those CLQ candidates that we followed up spectroscopically, we notice no overall difference between the light curves of CLQs versus non-CLQs.

4.1. Distribution of Luminosity Changes and Flux Ratios

The luminosity change at 3240 Å, calculated from the simple power-law continuum component from `QSfit` (Section 3.2), is plotted against the luminosity change of Hβ in Figure 3. The uncertainties were determined from the rms of model component fits from 100 Monte Carlo realizations of the data; then the errors in luminosity from both epochs are added in quadrature to compute the error in $|\Delta L|$. The flux changes are shown in the adjacent panel. There is a positive correlation between continuum change and BEL change, whether measured in luminosity or in flux.

The final CLQ sample is shown by red diamonds in Figure 3. We find that CLQs are interspersed throughout the entire distribution. There also exist cases where either the broad components did not vanish completely, despite substantial continuum luminosity change, or the signal to noise was not deemed sufficient for a CLQ classification (e.g., see Appendix A). When multiple follow-up spectra exist, the spectrum with highest S/N was chosen for the comparison with SDSS and is listed in Table 2. The resulting luminosities are given in Table 3.

To determine more clearly how the line varies relative to the continuum, we compute the flux ratio between the bright and dim states. If the flux ratios are proportional to each other, that would mean a constant EW and suggest a constant spectral energy distribution (SED) during the transition. Figure 4 shows

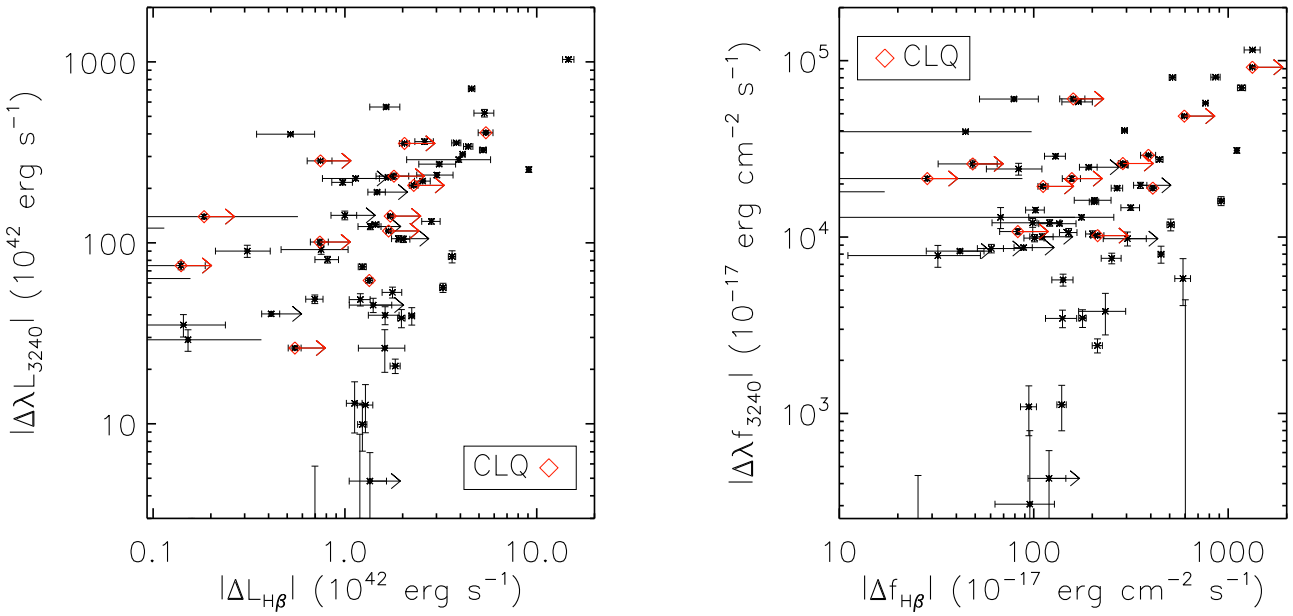

Figure 3. Absolute value of the 3240 Å continuum and Hβ change in luminosity (left panel) and flux (right panel) for all analyzed CLQ candidates with a median dim-state S/N near Hβ of > 5. The CLQs, defined as having absent broad Hβ at one epoch by at least $N_\sigma(\mathrm{H}\beta) > 3$, are over-plotted as red diamonds. Red horizontal arrows indicate lower limits on CLQs, corresponding to upper limits on the amount of Hβ flux.

the flux ratio $\lambda L_{3240,\mathrm{high}}/(\lambda L_{3240,\mathrm{low}})$ against $L_{\mathrm{H}\beta,\mathrm{high}}/L_{\mathrm{H}\beta,\mathrm{low}}$. We see that strong Balmer line variability is associated with the largest continuum variations. Given the number of lower limits and the large scatter, it is not clear whether the relative flux changes are proportional without a larger sample. The marginal distributions are shown for both axes so that the location of CLQs relative to the tail can more easily be seen. The CLQ fraction is displayed as a function of $\lambda L_{3240,\mathrm{high}}/(\lambda L_{3240,\mathrm{low}})$ in the right panel of Figure 4.

4.1.1. Highly Variable Quasars and Intermediate Transitions

Among the objects that do not exhibit strong BEL changes in the follow-up spectrum, in many cases this is due to a rebrightening since the last PS1 epoch, as revealed by CRTS photometry. Roughly half the observed cases were found to have recent brightening by several tenths of a magnitude. When excluding the rebrightened sources, we find a CLQ confirmation rate of 20% to 50% for flux deviations $N_\sigma(\mathrm{H}\beta) > 3$–1, respectively, from our follow-up.

Among the non-CLQs that did show a strong continuum change, in some, the BEL flux remained after clearly responding to the change in the continuum level—for example, J000116.00+141123.0 and J012946.71+150457.2 (Figures 1 and 5). In Section 4.2.5, we elaborate on the latter object. See Figure 8 for more objects with significant continuum and BEL variability that still retain a small portion of the broad Hβ line. For example, the object J233843.40-105719.5 in the last panel of Figure 8 lost all the 3240 Å power-law continuum flux. This object might be classified as a Type 1.8, since it still has broad Hα and a slight amount of broad Hβ in the dim state.

In several other candidates, Balmer BEL flux was retained in the dim state simply because the *fractional* luminosity change was relatively small (i.e., they were very luminous before dimming). For this reason, we find that the largest change in Hβ or 3240 Å luminosity is a non-CLQ (J025619.01−004501.3 at $z = 0.72$; Figure 3 left panel). However, this changes when instead considering the flux ratio between high and low states (Figure 4). Moreover, by comparing Figures 3 and 4, the CLQ fraction is more sensitive to the fractional continuum luminosity change rather than the absolute change.

4.2. Other Behavior and Objects of Interest

4.2.1. Strong He IIλ4686 Å Variability

Figure 2 (top panel) shows an example of a CLQ (J000904.54-103428.7) with vanishing BELs, and a particularly strong change in He IIλ4686 Å. In reverberation mapping studies of NGC 5548 (Fausnaugh et al. 2016), He II is seen to respond quickly and strongly to continuum variations, implying that the size of the He II emission region is very close to the ionizing continuum source. A strong He II change is also seen in Mkn 110 (Kollatschny & Bischoff 2002), and the source J013203 shown in Figure 5, although broad Hβ is still clearly present in the dim spectrum.

4.2.2. NLS1 AGN: J123359.12+084211.5

J123359.12+084211.5 (Figure 2) shows a remarkable change in Fe II emission in a NLS1 AGN. See Blanchard et al. (2017) for a similar spectral change in a NLS1. J123359.12+084211.5 has a relatively small continuum change and large Eddington ratio compared to the other CLQs, making it a noticeable outlier.

4.2.3. The Post-starburst Quasar J210200.42+000501.8

The source J210200.42+000501.8 (Figures 1 and 2) was classified in Cales et al. (2013) as a post-starburst quasar. The authors presented a follow-up spectrum taken prior to our MMT spectrum when the quasar was at an intermediate stage between the two spectra listed here, based on the light curve.

Table 3
Spectral Decomposition

SDSSJID	$L_{3240,\mathrm{SDSS}}$ (10^{42} erg s^{-1})	Error in $L_{3240,\mathrm{SDSS}}$ (10^{42} erg s^{-1})	$L_{\mathrm{H}\beta,\mathrm{SDSS}}$ (10^{42} erg s^{-1})	Error in $L_{\mathrm{H}\beta,\mathrm{SDSS}}$ (10^{42} erg s^{-1})	$L_{3240,2}$ (10^{42} erg s^{-1})	Error in $L_{3240,2}$ (10^{42} erg s^{-1})	$L_{\mathrm{H}\beta,2}$ (10^{42} erg s^{-1})	Error in $L_{\mathrm{H}\beta,2}$ (10^{42} erg s^{-1})
J000116.00+141123.0	509.9	7.2	7.02	0.22	184.1	5.1	1.77	0.05
J000904.54−103428.7	341.5	2.0	4.27	0.05	201.0	0.4	<2.55	0.03
J001113.46−110023.5	244.5	7.3	2.19	0.21	41.5	0.1	0.56	0.10
J001206.25−094536.3	644.5	5.4	4.08	0.28	158.4	9.2	<1.24	0.23
J001502.38−094439.1	133.2	3.0	1.95	0.08	52.4	1.7	1.14	0.08
J002311.06+003517.5	936.3	3.6	10.02	0.19	378.5	9.8	<4.92	0.29
J002450.50+003447.7	691.5	5.0	4.60	0.28	464.8	1.7	<5.74	0.25
J002627.89−101020.5	1040.9	20.8	9.96	0.91	884.6	37.7	4.76	2.24
J002714.21+001203.7	579.9	7.6	7.47	0.54	816.8	2.0	4.45	0.35
J004339.32+134436.5	215.6	5.6	6.60	0.30	8.3	0.0	<0.27	0.00
J005244.14+142807.1	590.4	17.8	6.95	0.47	288.8	0.3	12.45	1.50
J012821.43+151956.4	666.3	8.8	6.66	0.25	303.8	8.6	4.06	0.14
J012946.71+150457.2	568.4	6.8	12.57	0.19	314.4	5.7	3.47	0.14
J013203.46−093153.6	139.5	0.5	1.47	0.03	76.0	0.9	1.54	0.08
J013458.36−091435.4	771.6	4.7	6.35	0.13	365.6	2.0	0.92	0.46
J025505.68+002522.9	744.5	1.3	7.52	0.09	181.1	12.0	5.88	0.28
J025606.03+001634.8	316.3	8.7	3.47	0.34	503.8	6.4	4.52	0.21
J025619.01−004501.3	1594.1	23.2	19.87	0.93	562.3	12.1	5.24	0.34
J033702.66+010627.5	108.6	4.6	1.79	0.14	343.1	22.9	7.56	1.11

Note. The subscript "SDSS" denotes the earlier epoch, SDSS spectrum, and the subscript "2" denotes the follow-up spectrum. The full list of 109 fits are available in the electronic version.

(This table is available in its entirety in machine-readable form.)

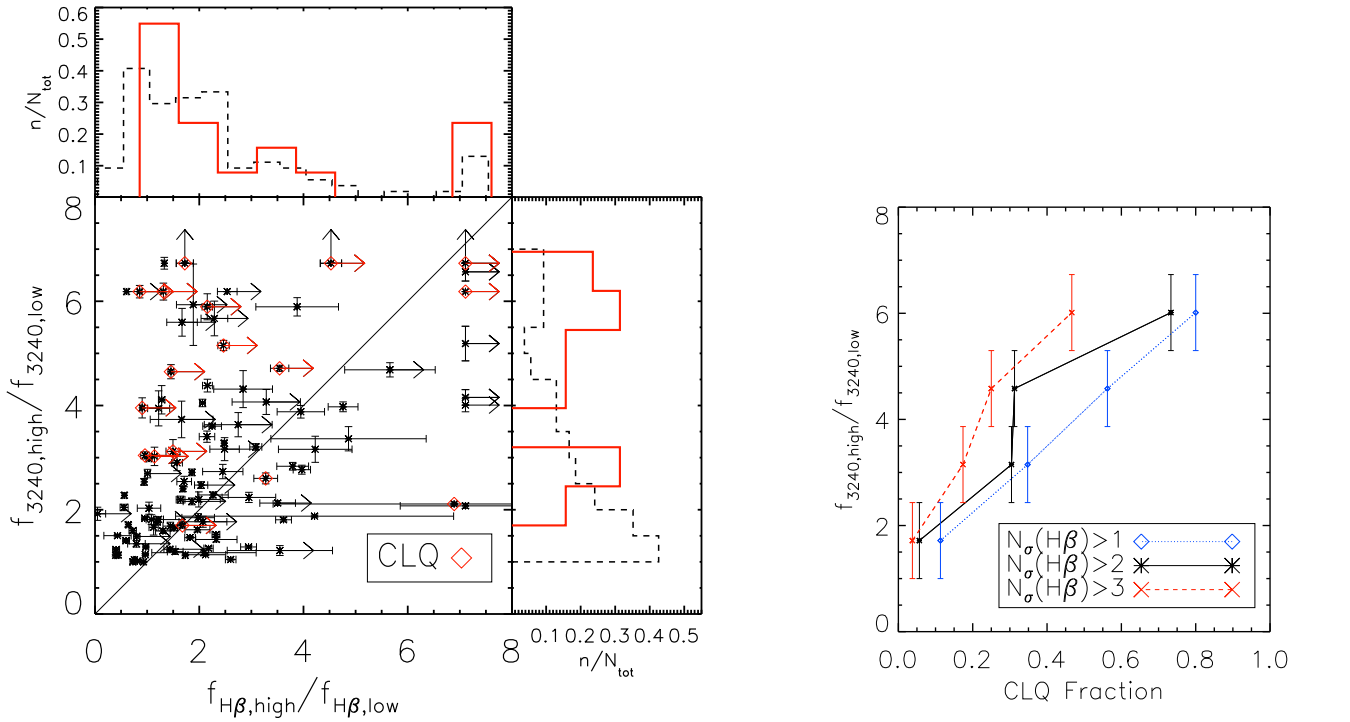

Figure 4. Left: flux ratio at the 3240 Å continuum versus the Hβ flux ratio for CLQ candidates. The CLQs are over-plotted as red diamonds (and arrows) as in Figure 3. The "high" and "low" Hβ fluxes are labeled according to the continuum level, so the ratios may sometimes be <1 if the continua are similar, possibly due to slightly inaccurate scaling of the follow-up spectrum. Black arrows indicate locations of objects that fell outside the plotted range due to small low-state flux levels. The line with unit slope is the expectation for a linear response of BEL flux to the continuum variability. The marginal distributions are shown on either axis, where CLQs are shown in red and the overall sample is the black dashed histogram. Right: CLQ fraction as a function of continuum flux ratio for three different thresholds in N_σ(Hβ).

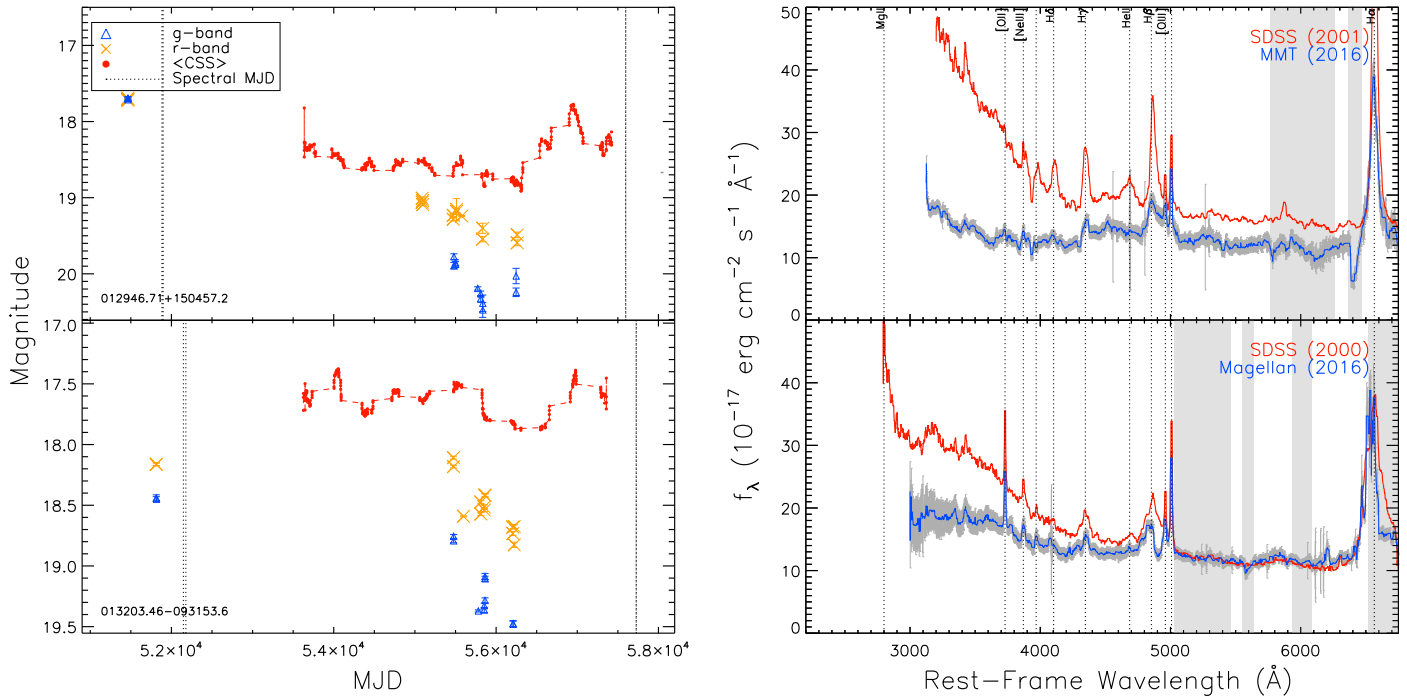

Figure 5. Left: SDSS, PS1, and CRTS light curves for CLQ candidates J013203 (top) and J012946 (bottom), observed 2016 December 4 with MMT and 2016 July 28 with *Magellan*, respectively. Right: repeat spectra for each source in the adjacent left panel. J013203 shows a disappearance of He II (see Section 4.2.1). J012946 shows an remarkable disappearance of the red half of the Balmer BELs with N_σ(Hβ) = 6 in response to a relatively large continuum change (Section 4.2.5).

The SDSS spectrum was obtained during a flaring event. Another dramatic CLQ, J101152.98+544206.4 (Runnoe et al. 2016), was found in a post-starburst galaxy, but the light curve bright phase exceeded a short-lived flare, leading the authors to conclude that it was not a tidal disruption event (TDE) or a supernova.

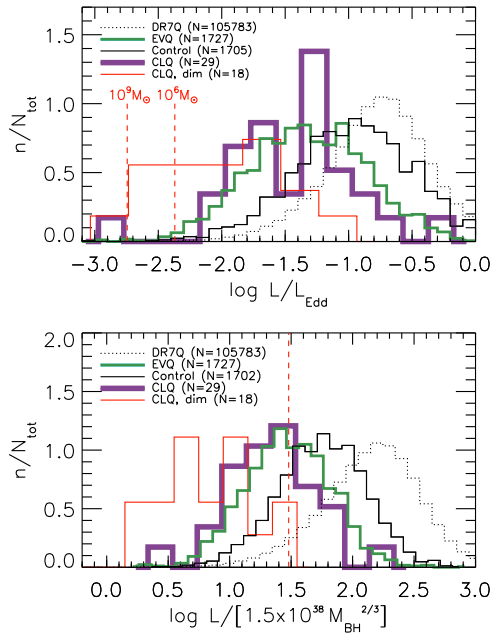

Figure 6. Top: the distribution of Eddington ratio for $z < 0.83$ extremely variable quasars in SDSS/PS1 (EVQs, our parent sample; in green), a less variable control sample matched in redshift and luminosity (in solid black), the full DR7 sample (dotted), and DR7 quasars with confirmed BEL changes (CLQs; in purple). The thin red histogram shows the distribution of the estimated dim-state values for CLQs that were analyzed in Section 3.2. Each histogram has been normalized to have unit area. Red vertical dashed lines indicate the predicted critical values from Nicastro (2000) above which BELs should be observable, for two different SMBH masses. Bottom: as in the top panel but for the quantity $\log(L_{\rm bol}/[1.5 \times 10^{38} M_{\rm BH}^{2/3}])$, similar to the Eddington ratio,where the BH mass is in units of solar masses (this particular way of expressing this quantity was chosen for simplicity). The quantity $L_{\rm bol}/M_{\rm BH}^{2/3}$ is the critical parameter in the disk-wind model of Elitzur & Ho (2009) and Elitzur et al. (2014) that determines whether or not a BLR can form. The red vertical dashed line indicates the predicted critical value above which BELs should be observable in this model.

4.2.4. Flickering CLQs J002311.06+003517.5 and J225240.37+010958.7

The objects J002311.06+003517.5 and J225240.37+010958.7 were both presented as CLQs in MacLeod et al. (2016). They both showed a significant dimming in PS1 since the latest BOSS spectra, so we observed them with *Magellan* in 2016 July and with MMT in 2017 October. The emerging and disappearing Balmer BELs appear to be associated with dramatic brightening and dimming in the light curves, and they have recently turned off again (see Figures 2 and 7). J225240.37+010958.7 has a boxy Hβ profile (see Section 4.2.5) and exhibits only one dramatic flare over the course of the light curve, whereas J002311.06+003517.5 shows persistent large-amplitude variability throughout its light curve.

4.2.5. Asymmetric Broad Balmer Line Profiles

The following sources displayed asymmetric, boxy, or velocity-shifted broad Balmer emission lines. These are rare features seen usually in low-luminosity quasars, and are interesting because they may indicate a rotating disk (e.g., Strateva et al. 2003) or a supermassive black hole binary (Runnoe et al. 2017). In general, where detectable, the Hβ and Hα profiles behaved similarly, but the Mg II profile did not behave in the same way as the Balmer line profiles.

1. J141213.61+021202.1 (Figure 7): This object has lost the broad Hβ component by a factor of 1.43 in flux (although at a $<2\sigma$ level per spectral pixel), with a relatively small continuum change of a factor 1.24. In the earlier (bright) state, the broad component was significantly *blueshifted* relative to the narrow component.
2. J220537.71-071114.5 (Figure 2): This CLQ exhibits a *redshifted* broad Hβ component in the bright state, before it disappears completely. It also displays a down-turn of the UV part of the spectrum, possibly similar to the change seen in J1100-0053 (Ross et al. 2018).
3. J012946.71+150457.2 (Figure 5): This source maintained a blue contribution to the broad Balmer lines among both (bright and dim) states, but loses the *red half* of the BEL in the later dim state. This behavior is very rare among AGN. The strong change in BEL luminosity is evident in Figure 3, where the luminosity change is nearly $|\Delta L_{\rm H\beta}| = 9 \times 10^{42}$ erg s^{-1}.
4. J143455.31+572345.0 (Figure 2): This object is listed as a disk-emitter (DE) quasar in Strateva et al. (2003) and therefore is targeted as a DE QSO by the TDSS few-epoch-spectroscopy program (described in MacLeod et al. 2018).
5. There are additional examples of boxy or asymmetric Balmer profiles in our sample; for example, in Section 4.2.4, we described the CLQ J225240.37+010958.7, which has a noticeably extended red wing in the Hβ profile. The object J224829.47+144418.0 shown in Figure 7 shows a very similar profile. A more detailed analysis is needed to classify all of them, which is outside the scope of this work. In particular, we are unable to determine whether boxy profiles are more or less frequent among the CLQ population because we lack a good benchmark sample to compare with, and the line profiles of CLQs may change shape as they dim, which would not generally be detectable given the dim-state S/N typical here. A time-resolved transition between states would be especially useful in searching for emerging boxy profiles in dimming CLQs. We defer further discussion of profile shapes to a future paper.

4.3. Distribution of Eddington Ratios

The Eddington ratio is an important physical quantity that has been found to drive many features of quasar spectra and time variability. To test for any trend with Eddington ratio, we follow the procedure in Rumbaugh et al. (2018) of constructing a less variable (non-EVQ) control sample and comparing the Eddington ratio distributions. In particular, for each quasar in the highly variable ($\Delta g > 1$ mag, $\Delta r > 0.5$ mag) sample, we select a quasar at similar redshift and luminosity that does not meet the variability threshold, and form a control sample. Our results indicate that CLQs are indeed at lower Eddington ratios than the control sample (Figure 6). Values of $L/L_{\rm Edd}$ from Shen et al. (2011) are adopted for each source, so the distribution shown is mostly for the bright-state spectra, although a handful of values will be for the dim state (e.g., J233317 from MacLeod et al. 2016, which has $\log(L/L_{\rm Edd}) = -2.97$). The 3240 Å continuum luminosity typically changes by a factor of four, so the bolometric luminosity (and therefore Eddington ratio) will be significantly smaller for the dim-state spectra. We estimate the Eddington ratios in the dim state by simply

dividing the DR7 values by the amount that the 3240 Å continuum luminosity has dimmed, based on our spectral decomposition described in Section 3.2. The thin red histogram shows the distribution of the estimated dim-state values for CLQs that were analyzed in Section 3.2. Note that the bolometric luminosity may have dimmed by a larger amount than the 3240 Å continuum, so the red histogram is only a rough estimate of the true distribution of Eddington ratios in the dim state.

In Elitzur & Ho (2009) and Elitzur et al. (2014), the quantity $L_{\rm bol}/M_{\rm BH}^{2/3}$ was found to be the critical parameter in a disk-wind model that determines whether or not a BLR can form. The bottom panel of Figure 6 shows the distribution of this quantity for the same subsamples as in the top panel. The vertical red dashed line shows the critical value that divides Type 1 and true Type 2 AGN.

We discuss the implications of this analysis in Section 5.1.

5. Discussion

The two fundamental questions we can address are: (a) What is the CLQ rate among highly variable AGN? (b) Is the loss or emergence of BEL flux in CLQs due to a rare and different physical mechanism than that causing variability in the overall population of quasars? We find a CLQ confirmation rate among highly variable quasars of 20%, dependent on our luck with the timing of follow-up observations for some objects. While the CLQ fraction among highly variable quasars was estimated to be $>$ 15% in MacLeod et al. (2016), they took the ratio of CLQs to the *total* number of highly variable quasars (on timescales of ∼8 yr rest frame), regardless of the timing of the SDSS and BOSS spectral epochs. For our follow-up, we generally only target those quasars that are currently at least 1 mag brighter or dimmer compared to the g-band magnitude near any previous spectral epochs.

We also find that strongly varying quasars often show a large contrast in Balmer BELs between dim and bright states, so when defining CLQs simply based on (dis)appearing broad Hβ, the resulting CLQ fraction is highly dependent on the significance of the change, N_σ(Hβ). In terms of the flux ratio, CLQs are among those variables with the largest changes, with the CLQ fraction increasing from 10% to roughly half as the continuum flux ratio between states at 3420 Å increases from 1.5 to 6.

Based on this analysis, CLQs are consistent with being simply the tail of a continuous distribution of quasar variability episodes. However, the sample would benefit from a much larger size, especially at the highly variable tail, to address this question. We discuss the possibilities in Section 5.2. Our results indicate that CLQs in the dim state have lost a substantial fraction of their continuum luminosity compared to other quasars. It is clear that this aspect causes the BLR to react significantly, possibly structurally, to the continuum change.

The "flickering" CLQs J225240.37+010958.7 and J002311.06+003517.5 (Section 4.2.4) show that objects with substantial broad BEL variability appear to repeat this behavior whenever the continuum varies significantly. Similar persistent variability has also been seen in SDSS J022556 (MacLeod et al. 2016) and Mkn 1018 (Husemann et al. 2016). Furthermore, Rumbaugh et al. (2018) find longer characteristic timescales and larger variability amplitudes, *as measured from SDSS S82*, for the sample of EVQs found in DES/SDSS data. This result makes sense in view of the red noise variability power spectrum of quasars, where the power index of −2 toward higher frequencies leads to larger variability amplitudes on longer timescales. These findings suggest that previously identified strong variability predicts the same behavior in the future. It is possible that a small fraction of the CLQs presented here and elsewhere exhibit physically distinct variability from the rest of quasar population, but that most of the CLQs are actually just the extreme tail of regular quasar variability. Here, we discuss the physical properties of CLQs on average, and leave a detailed analysis for particular sources for future study.

5.1. Physical Origin of CLQ Variability

Studies have investigated whether disappearing BELs in the optical are likely to originate from extrinsic or transient events (e.g., Goodrich 1989, 1990; LaMassa et al. 2015; Merloni et al. 2015; Ruan et al. 2016; Runnoe et al. 2016; Gezari et al. 2017). In MacLeod et al. (2016), we found that variable extinction by dust cannot account for BEL flux changes relative to the continuum in CLQs, nor the observed timescales. In general, the flares are longer lived than the typical TDE (Guillochon et al. 2014), and pre-existing narrow emission lines in CLQ spectra are not expected for a single TDE outburst. The CLQs studied here are all $z < 1$ and lack foreground spectral features, so their variability is unlikely to be the result of lensing by a foreground galaxy (see, e.g., Quimby et al. 2014). Furthermore, erratic variability and multiple flaring episodes are evident in the light curves of CLQs, as opposed to single Paczyński curves one might expect for high-amplitude microlensing by a single foreground star in a faint foreground galaxy (Bruce et al. 2017). Therefore, extreme variability is likely intrinsic to the quasar and not due to lensing.

We are now able to specifically confirm a trend with Eddington ratio from our follow-up spectroscopy, and it is consistent with the well known anti-correlation between Eddington ratio and variability amplitude (e.g., Wilhite et al. 2008; MacLeod et al. 2010). We find that CLQs have lower Eddington ratios than a control sample matched in redshift and luminosity, as suggested by Rumbaugh et al. (2018). Since CLQs seem to occupy this region of physical parameter space, as Rumbaugh et al. point out, BEL (dis)appearance in general is not likely to be due to variable obscuration, TDEs, or microlensing by foreground stars, unless these events are strongly preferred in quasars with lower Eddington ratio.

Interestingly, the CLQs are found near the critical luminosity below which the BLR disappears (Elitzur & Ho 2009, vertical line in bottom panel of Figure 6). This supports a picture where the accretion rate in CLQs is barely enough to support a broad line region, assuming a disk-wind model for the BLR. Nicastro (2000) also assume a disk-wind model and derive a critical threshold in $L_{\rm bol}/L_{\rm Edd}$ for BLR disappearance as a function of black hole mass (vertical lines in top panel of Figure 6). Here, we assume a maximum accretion efficiency of $\eta = 0.06$ and a viscosity coefficient of $\alpha = 0.1$ as in Nicastro (2000). The CLQs begin to reach this threshold if we estimate $L_{\rm bol}/L_{\rm Edd}$ in the dim state (conservatively assuming the same SED as in the bright state). Assuming the variability is indeed due to an accretion rate change, and that the estimated dim-state values for CLQs as well as the adopted values for η and α are not too inaccurate, our results indicate that the Elitzur & Ho (2009) model for the disk-wind BLR may provide a good description of CLQs, as the CLQ distribution would need to be a factor of 10 lower in $L_{\rm bol}/L_{\rm Edd}$ before reaching the Nicastro (2000)

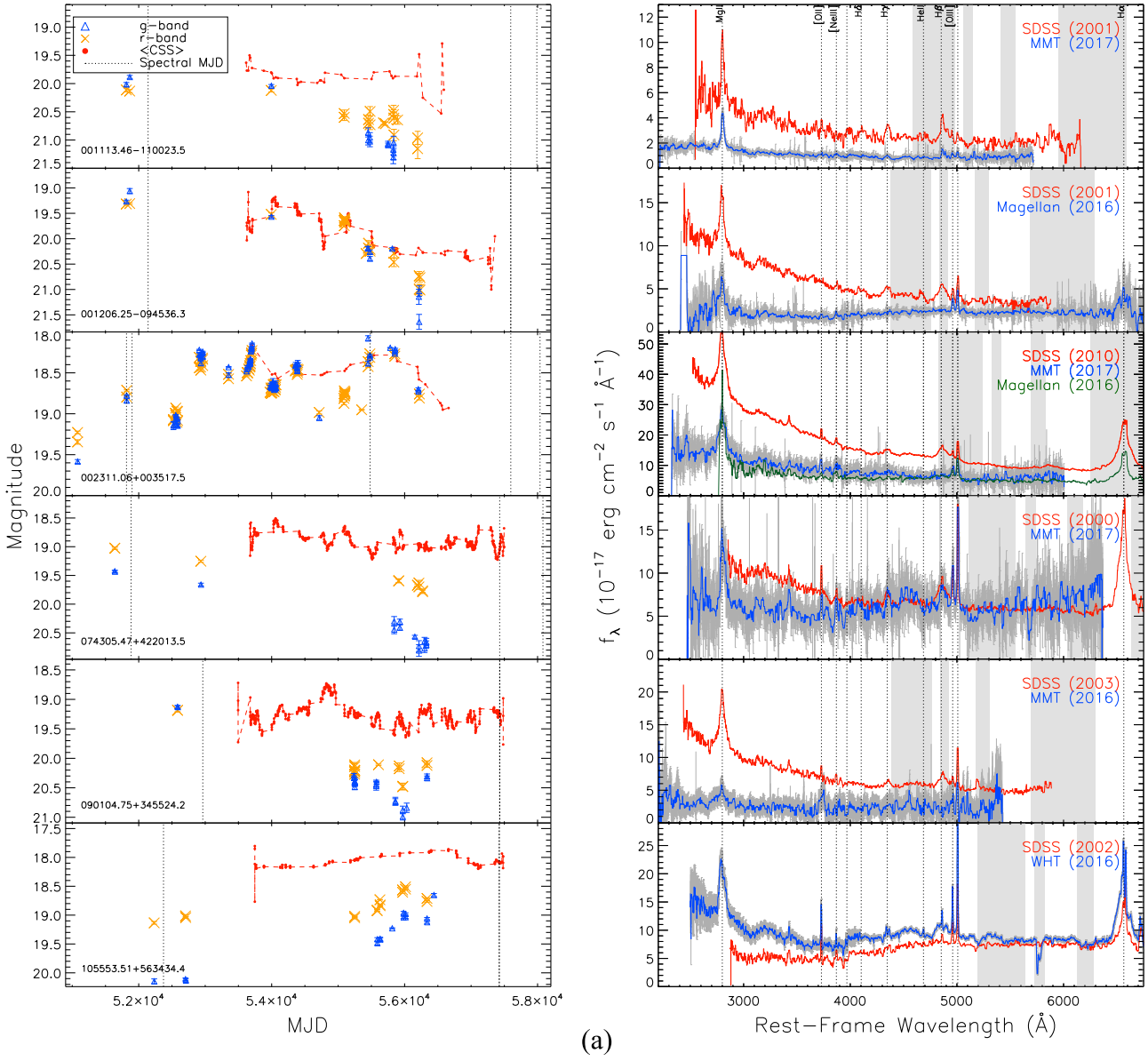

Figure 7. As in Figure 2, but for lower-significance CLQs with $1 < N_\sigma(\mathrm{H}\beta) < 3$. Light curves and repeat spectra shown in R.A. order. Left: SDSS and Pan-STARRS g-band photometry is shown as blue triangles. Red data points show archival photometry from CRTS. The existing spectroscopic epochs are indicated by the vertical lines. Right: existing spectra for objects in the adjacent left panel (red is SDSS; blue or green is our follow-up), corrected for telluric absorption where needed.

critical threshold between quasars that do and do not have a BLR.

Understanding the various physical processes that occur at low accretion rates is therefore highly relevant to the study of changing-look variability. A key question is how to connect the observed timescales for CLQ transitions with theoretical timescales for accretion disks. The expected timescale for a major accretion rate change is the viscous timescale (Krolik 1999). However, the expected viscous timescale in the optical-emitting region of the disk is orders of magnitude longer than what is observed for CLQ transitions (for a summary of the timescale problem, see Lawrence 2012). Various solutions to the problem of observed transition timescales have been proposed, some involving thermal instabilities, as we discuss later. The results from Husemann et al. (2016) on Mkn 1018 indeed support a disk temperature change associated with the CLQ event, based on the measured temperature in both states and corresponding luminosity dependence. Additionally, the timescale is consistent with a thermal timescale for an accretion disk. Other theoretical timescales include the dynamical and sound-crossing time; the former is usually too short to explain the observations, whereas the radial sound-crossing time is usually too long (e.g., see table in Lawrence 2016). Either the instability (or instabilities) must propagate throughout the disk far faster than the viscous timescale, such as over a thermal timescale, or our calculation of a viscous timescale is off by orders of magnitude.

State of the art simulations of the thermal instability in the radiation-dominated region of accretion disks by Jiang et al. (2016) indicate that disks with lower-metallicity gas are more prone to thermal instability, as the iron opacity bump is less effective as a stabilizing mechanism. Therefore, a reliable way

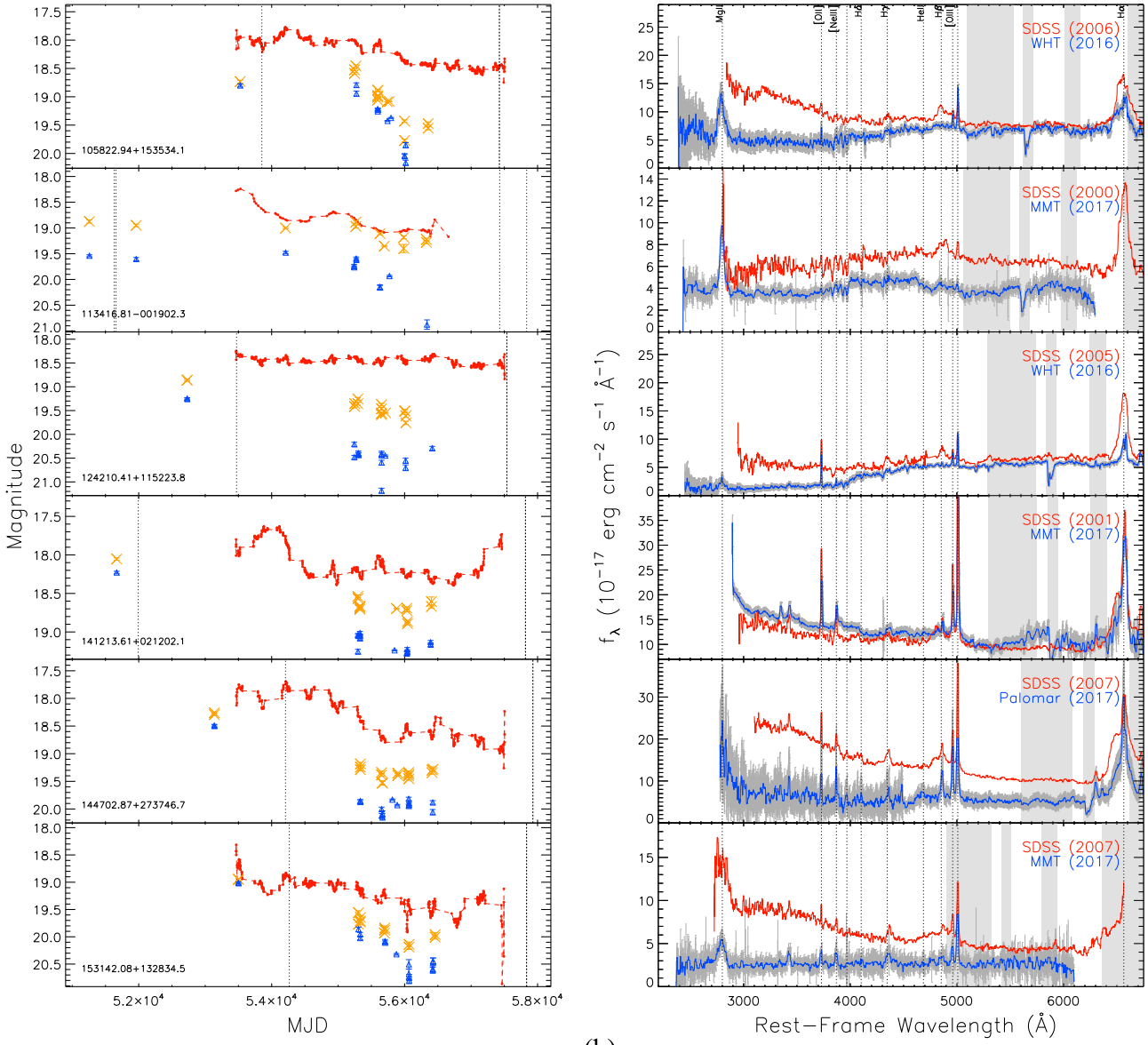

(b)

Figure 7. (Continued.)

to measure the metallicity in the inner regions of quasars may be relevant to the interpretation of CLQs.

A recent idea that would explain the fast CLQ variability invokes a cooling front due to a sudden change in torque applied by the magnetic field at the inner-most stable circular orbit (Ross et al. 2018; Stern et al. 2018). Another idea involves an advection-dominated accretion flow (ADAF; Noda & Done 2018). In the latter scenario, the BLR disappearance is triggered by a sudden drop in accretion rate, leading to an ADAF in the inner disk; the consequence is a harder SED. Dexter & Begelman (2019) suggested that all quasar accretion disks are actually magnetically elevated, leading to larger scale heights and shorter variability timescales than expected in standard thin disk theory (Shakura & Sunyaev 1973). In this case, CLQs may simply be the tail of a continuous distribution of quasar variability.

Multi-wavelength observations for more CLQs are needed, as the SED can suggest certain physical environments. For example, X-ray repeat spectroscopy for a handful of sources rules out variable absorption as the cause of variability (LaMassa et al. 2015, and references therein), as well as do mid-IR light curves (e.g., Ross et al. 2018; Stern et al. 2018). One of the best studied sources, NGC 2617 (Shappee et al. 2014), has simultaneous UV–IR monitoring along with X-rays that show reprocessed emission from a central X-ray source with no signs of dust obscuration along the line of sight to the central engine. Through SED modeling, Kubota & Done (2018) determined that X-ray reprocessing becomes increasingly important at lower accretion rates, but it cannot account for all the optical-UV variability in SDSS quasars.

5.2. Future Work

Our sample is dominated by dimming events (or "turn-off" CLQs) because of the sample construction: because our parent sample is the DR7 quasar catalog, most have broad BELs in the early state. Only two of the CLQs presented here are transitioning to a bright state (J105553.51+563434.4 and

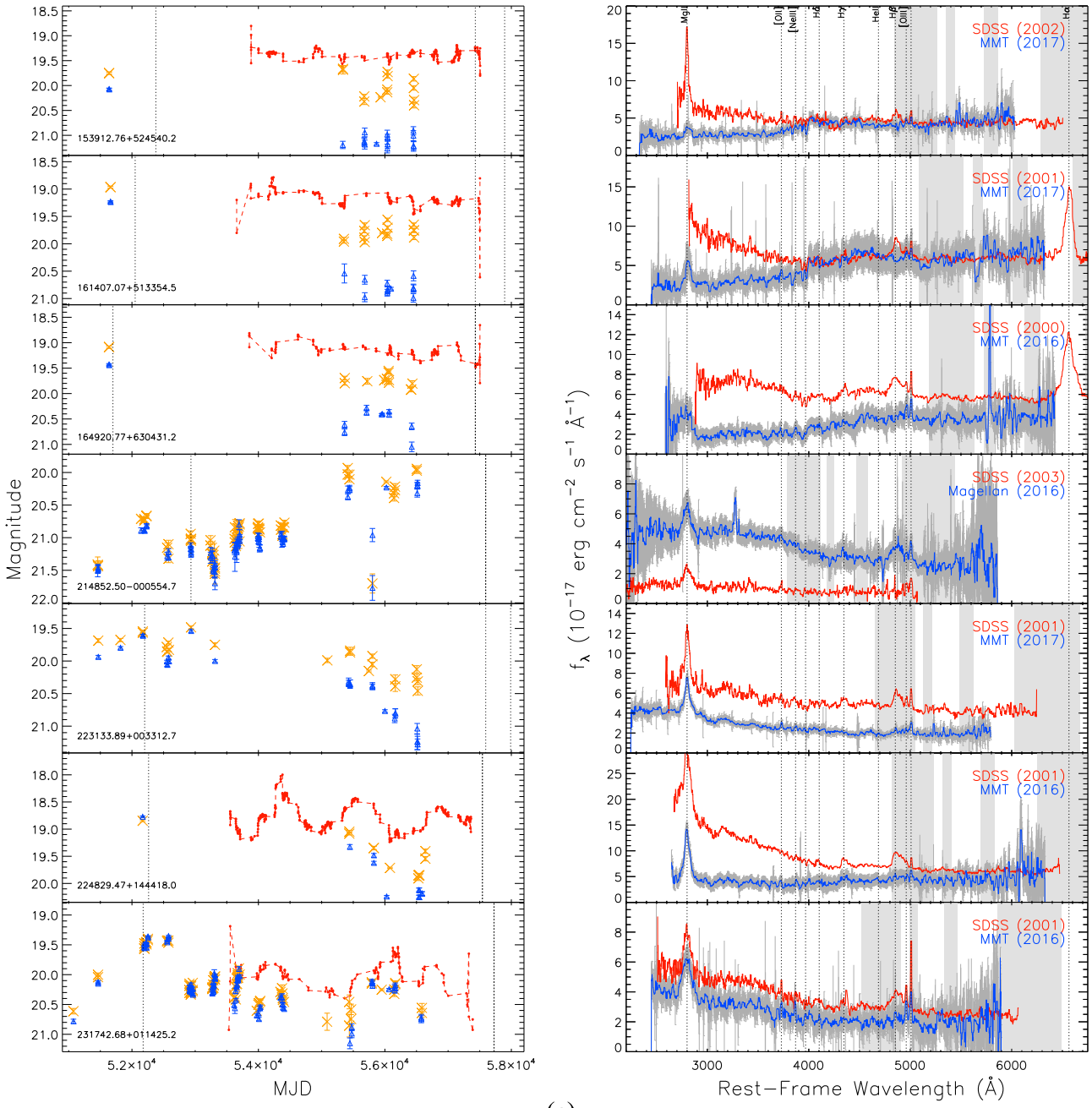

(c)

Figure 7. (Continued.)

J214852.50−000554.7; Figure 7). The turn-off CLQ frequency is likely balanced by turn-on events, unless we expect the population to be evolving. A major piece of future work is therefore to establish a suitable parent sample and method for searching for turn-on events. The challenge in starting from a galaxy catalog is how to produce reliable photometry for just the (mildly active) nuclei of extended galaxies, as well as how to efficiently sift through a sample an order of magnitude larger than the quasar sample. For a recent effort, see Drake et al. (2019).

Another outstanding question is why the Mg II BEL, formed at a similar ionization energy as the Balmer lines, is generally less responsive to strong changes in the continuum (see also Cackett et al. 2015). Given that reverberation mapping studies in the past have typically focused on lower-redshift quasars, where Mg II is outside the optical wavelength range (although see Shen et al. 2016), characterizing the response of the Mg II line is an important goal. We leave the Mg II BEL variability measured from these follow-up spectra for a future publication (D. Homan et al. 2019, in preparation).

Having well-sampled light curves for quasars is essential for determining the timescales associated with the transitions and for selecting targets for follow-up. Therefore, future multi-band surveys in the time domain such as the Large Synoptic Survey Telescope (Ivezic et al. 2008; LSST Science Collaboration et al. 2009), PS2 (Chambers 2014), Zwicky Transient Facility (ZTF; Bellm 2014), as well as, for brighter AGN, the ongoing All-Sky

Automated Survey for SuperNovae (ASASSN; Shappee et al. 2014), should provide many interesting targets for contemporaneous spectroscopic follow-up. For example, ZTF commenced in 2018 March and is monitoring 15,000 $\deg^2$ of the Northern Sky in g and r bands with a cadence of 3 nights down to a magnitude of 20.5 mag over a baseline of 3 yr. While we can predict which variability episodes are uncommon with respect to the overall quasar population (e.g., Graham et al. 2017), one issue is how to efficiently flag CLQs in photometric monitoring data *before* they change, so that we can spectroscopically monitor them in the optical *during* the transition. Predictive modeling, where the expected variability is predicted either for a given night or over a particular timeframe, could prove useful here (see Graham et al. 2019).

It is unclear whether the same physical processes are occurring in/around the accretion disks in EVQs. But there are some hints of outliers and interesting objects; this problem will also be easier to solve with larger data sets of repeat quasar spectroscopy. Samples have recently grown substantially in the SDSS-IV TDSS (Morganson et al. 2015; MacLeod et al. 2018), forming a pilot to even larger spectroscopic surveys upcoming in SDSS-V (Kollmeier et al. 2017). A sample of newly discovered CLQs from SDSS-IV will be presented in C. MacLeod et al. (2019, in preparation). The ideal survey would provide dense cadence repeat spectroscopy of a large sample of quasars—for example, via time domain objective prism survey, or a many-band space mission such as SPHEREx (Doré et al. 2018) or the Time-domain Spectroscopic Observatory.[17] One potential result from a large survey of repeat quasar spectroscopy is to expand the sample size of CLQs with multiple spectra before, during, and after the transition. With a larger sample size, we can detect and characterize discontinuities in the overall variability distributions associated with CLQ behavior.

This material is based upon work supported by the National Science Foundation under grant Nos. AST-1715763 and AST-1715121. The work of D.S. was carried out at the Jet Propulsion Laboratory, California Institute of Technology, under a contract with NASA. We thank Marco Lam and Nigel Hambly for assistance with the PS1 DVO database hosted at Edinburgh. We thank Peter Blanchard for assistance in carrying out Blue Channel observations. C.L.M. would like to acknowledge Zeljko Ivezic, Martin Elvis, and Fabrizio Nicastro for useful discussions regarding the Eddington ratio and disk-wind model. We thank the anonymous referee for their very helpful and thorough comments.

Funding for the SDSS and SDSS-II has been provided by the Alfred P. Sloan Foundation, the Participating Institutions, the National Science Foundation, the U.S. Department of Energy, the National Aeronautics and Space Administration, the Japanese Monbukagakusho, the Max Planck Society, and the Higher Education Funding Council for England. The SDSS website is http://www.sdss.org/.

The SDSS is managed by the Astrophysical Research Consortium for the Participating Institutions. The Participating Institutions are the American Museum of Natural History, Astrophysical Institute Potsdam, the University of Basel, the University of Cambridge, Case Western Reserve University, the University of Chicago, Drexel University, Fermilab, the Institute for Advanced Study, the Japan Participation Group, Johns Hopkins University, the Joint Institute for Nuclear Astrophysics, the Kavli Institute for Particle Astrophysics and Cosmology, the Korean Scientist Group, the Chinese Academy of Sciences (LAMOST), Los Alamos National Laboratory, the Max-Planck-Institute for Astronomy (MPIA), the Max-Planck-Institute for Astrophysics (MPA), New Mexico State University, Ohio State University, the University of Pittsburgh, the University of Portsmouth, Princeton University, the U.S. Naval Observatory, and the University of Washington.

Funding for SDSS-III has been provided by the Alfred P. Sloan Foundation, the Participating Institutions, the National Science Foundation, and the U.S. Department of Energy Office of Science. The SDSS-III website is http://www.sdss3.org/.

SDSS-III is managed by the Astrophysical Research Consortium for the Participating Institutions of the SDSS-III Collaboration, including the University of Arizona, the Brazilian Participation Group, Brookhaven National Laboratory, Carnegie Mellon University, the University of Florida, the French Participation Group, the German Participation Group, Harvard University, the Instituto de Astrofisica de Canarias, the Michigan State/Notre Dame/JINA Participation Group, Johns Hopkins University, Lawrence Berkeley National Laboratory, Max Planck Institute for Astrophysics, Max Planck Institute for Extraterrestrial Physics, New Mexico State University, New York University, Ohio State University, Pennsylvania State University, the University of Portsmouth, Princeton University, the Spanish Participation Group, the University of Tokyo, the University of Utah, Vanderbilt University, the University of Virginia, the University of Washington, and Yale University.

The Pan-STARRS 1 Surveys (PS1) have been made possible through contributions of the Institute for Astronomy, the University of Hawaii, the Pan-STARRS Project Office, the Max-Planck Society and its participating institutes, the Max Planck Institute for Astronomy, Heidelberg and the Max Planck Institute for Extraterrestrial Physics, Garching, Johns Hopkins University, Durham University, the University of Edinburgh, Queen's University Belfast, the Harvard-Smithsonian Center for Astrophysics, the Las Cumbres Observatory Global Telescope Network Incorporated, the National Central University of Taiwan, the Space Telescope Science Institute, the National Aeronautics and Space Administration under grant No. NNX08AR22G issued through the Planetary Science Division of the NASA Science Mission Directorate, the National Science Foundation under grant No. AST-1238877, the University of Maryland, and Eotvos Lorand University (ELTE).

The CSS survey is funded by the National Aeronautics and Space Administration under grant No. NNG05GF22G issued through the Science Mission Directorate Near-Earth Objects Observations Program. The CRTS survey is supported by the U.S. National Science Foundation under grants AST-0909182 and AST-1313422.

Facilities: SDSS, Pan-STARRS, WHT, MMT, Magellan, SO:Schmidt, SO:1.5m, SO:1m, Palomar.

Software: pyDIS, QSfit, pyRAF, MySQL/CASJobs.

Appendix A
Less-significant CLQs and Near CLQs

We show in Figure 7 the visually identified CLQs with relatively low significance, in the range $1 < N_\sigma(\mathrm{H}\beta) < 3$. In Figure 8, we present some examples where the Hβ line lost much of its broad component along with some dimming of the continuum, but not enough to classify it as a CLQ.

[17] https://pcos.gsfc.nasa.gov/physpag/probe/TSO-Probe-WhitePaper-submit.pdf

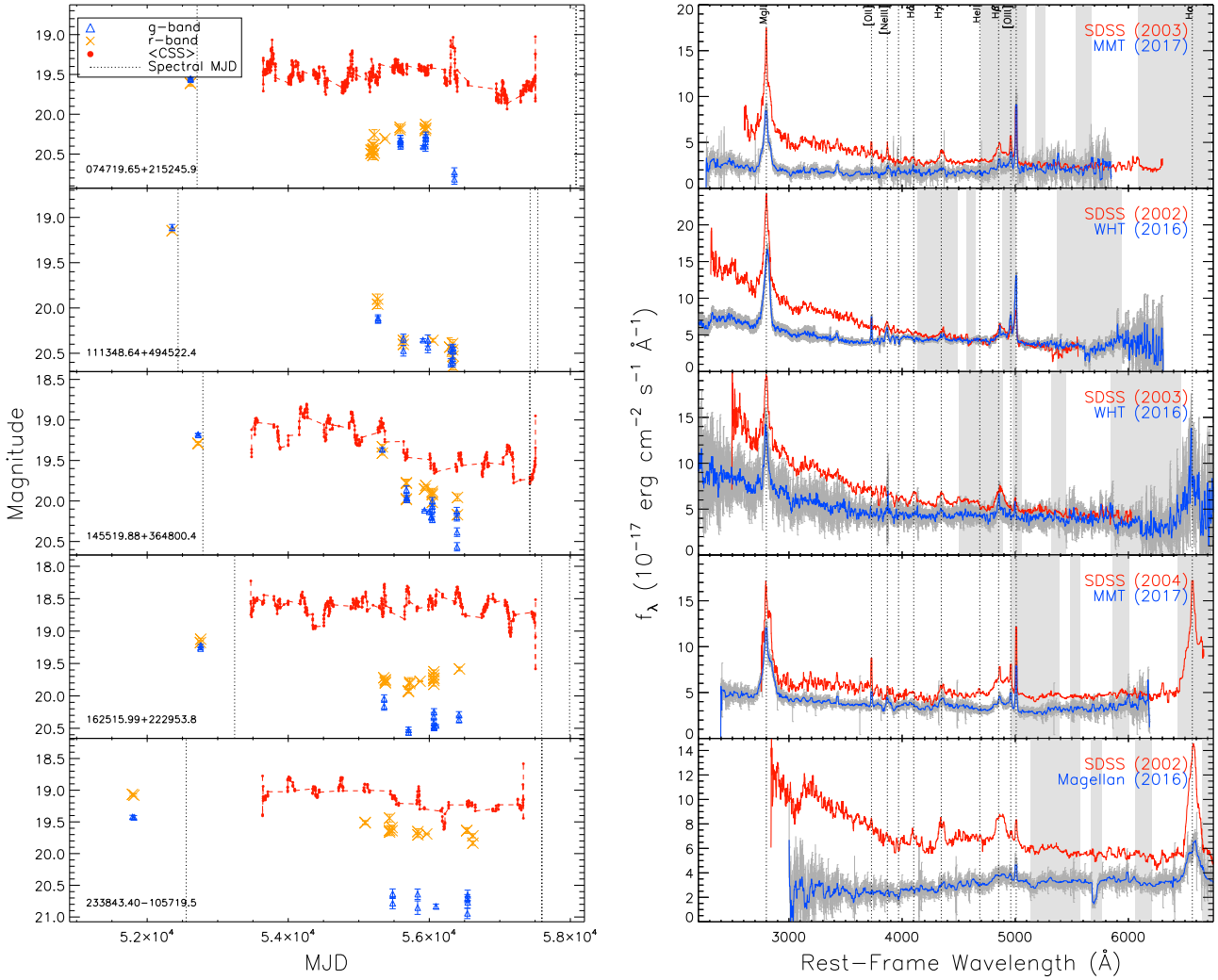

Figure 8. Near-CLQs from WHT/MMT/*Magellan*. See the caption for Figure 2.

Appendix B
Previously Missed Archival, Serendipitous CLQ

In MacLeod et al. (2016), we performed a systematic search for CLQs among quasars with repeat archival spectra in SDSS/BOSS. There, we only inspected objects that had both SDSS and BOSS epochs, unless the object was in S82; then we inspected all epochs, even if they were all in earlier SDSS (pre-BOSS). One source, J115355.88+112554.2, had two early SDSS spectral epochs that already confirm the object as a CLQ (see Figure 9). Although this object was missed by the MacLeod et al. (2016) selection since it lacks a BOSS epoch and is not in S82, it was selected as a CLQ candidate in the present work.

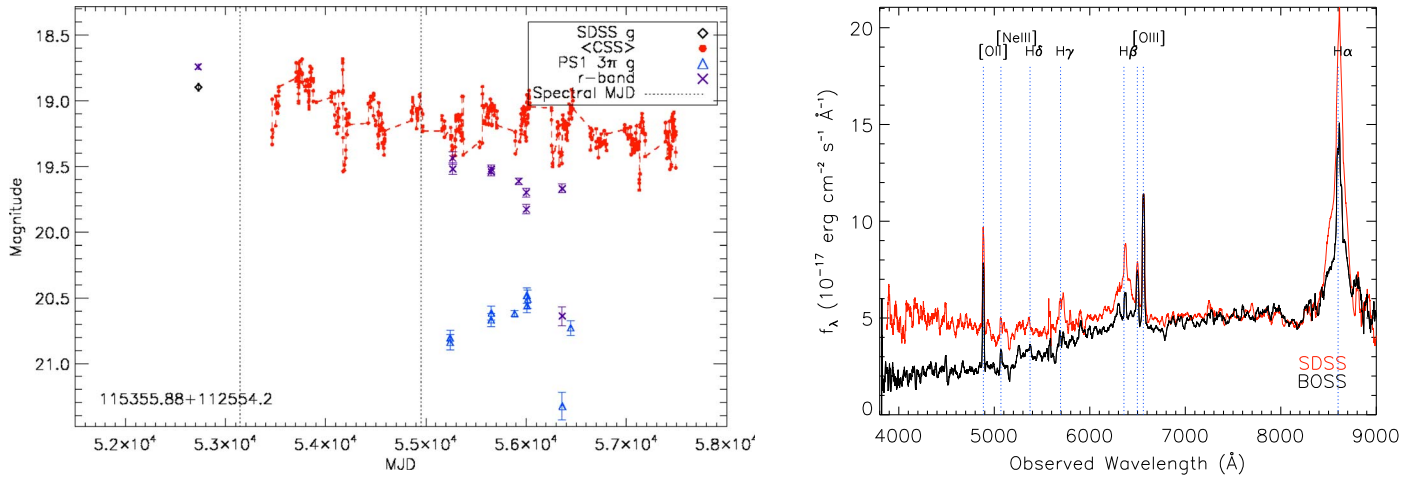

Figure 9. Left: light curve for a serendipitous CLQ J115355.88+112554.2 at $z = 0.31$ missed by the MacLeod et al. (2016) search. The existing spectroscopic epochs are indicated by the vertical lines. Right: existing SDSS and BOSS spectra. The BOSS flux has been scaled so that the [O III]λ5007 Å flux matches that in the SDSS spectrum.

Appendix C
Comparison to Published CLQs

SDSS J141324+530527.0 (SBS 1411+533) at $z = 0.456$ (Wang et al. 2018) is present in DR7Q, but was not selected as a candidate CLQ here since it only shows a magnitude change of -0.86 ± 0.05 in g from SDSS to PS1. SDSS J012648.08 −083948.0 (Ruan et al. 2016) would also be missed by this selection since it only varied by $\Delta g = 0.78$ mag, but it was not in our parent sample since (a) it is not in DR7Q and (b) it has a BOSS spectrum. SDSS J233602.98+001728.7 (Ruan et al. 2016) is not present in DR7Q, nor is the CLQ iPTF 16bco (Gezari et al. 2017) or the CLQs from Yang et al. (2018). SDSS J101152.98 +544206.4 (Runnoe et al. 2016), as well as the CLQs from MacLeod et al. (2016), meet the selection criteria here but already had confirming BOSS spectra, so we did not follow them up (except for the two that turned back off, described in Section 4.2.4). However, we list the CLQs from Runnoe et al. (2016) and MacLeod et al. (2016) in Table 2 for completeness. The CLQ WISE J105203.55+151929.5 (Stern et al. 2018) is present in DR7Q and is selected here as a CLQ candidate, though we did not perform follow-up photometry for this source.

ORCID iDs

Paul J. Green https://orcid.org/0000-0002-8179-9445
Michael Eracleous https://orcid.org/0000-0002-3719-940X
Matthew Graham https://orcid.org/0000-0002-3168-0139
David Homan https://orcid.org/0000-0002-4431-0890
John J. Ruan https://orcid.org/0000-0001-8665-5523
Jessie Runnoe https://orcid.org/0000-0001-8557-2822
Daniel Stern https://orcid.org/0000-0003-2686-9241
William Burgett https://orcid.org/0000-0003-4401-9582
Kenneth C. Chambers https://orcid.org/0000-0001-6965-7789
Nick Kaiser https://orcid.org/0000-0001-6511-4306
Eugene Magnier https://orcid.org/0000-0002-7965-2815
Nigel Metcalfe https://orcid.org/0000-0001-9034-4402

References

Abazajian, K. N., Adelman-McCarthy, J. K., Agüeros, M. A., et al. 2009, ApJS, 182, 543
Aihara, H., Allende Prieto, C., An, D., et al. 2011, ApJS, 193, 29
Anderson, S. F., Voges, W., Margon, B., et al. 2003, AJ, 126, 2209
Assef, R. J., Prieto, J. L., Stern, D., et al. 2018, ApJ, 866, 26
Becker, R. H., White, R. L., & Helfand, D. J. 1995, ApJ, 450, 559
Bellm, E. 2014, in The Third Hot-wiring the Transient Universe Workshop, ed. P. R. Wozniak et al., 27
Bentz, M. C., Peterson, B. M., Pogge, R. W., & Vestergaard, M. 2009, ApJL, 694, L166
Bischoff, K., & Kollatschny, W. 1999, A&A, 345, 49
Blanchard, P. K., Nicholl, M., Berger, E., et al. 2017, ApJ, 843, 106
Bruce, A., Lawrence, A., MacLeod, C., et al. 2017, MNRAS, 467, 1259
Cackett, E. M., Gültekin, K., Bentz, M. C., et al. 2015, ApJ, 810, 86
Calderone, G., Nicastro, L., Ghisellini, G., et al. 2017, MNRAS, 472, 4051
Cales, S. L., Brotherton, M. S., Shang, Z., et al. 2013, ApJ, 762, 90
Chambers, K. C. 2014, AAS/DPS Meeting, 46, 214.06
Chambers, K. C., Magnier, E. A., Metcalfe, N., et al. 2016, arXiv:1612.05560
Cohen, R. D., Puetter, R. C., Rudy, R. J., Ake, T. B., & Foltz, C. B. 1986, ApJ, 311, 135
Dawson, K., Schlegel, D. J., Ahn, C. P., et al. 2013, AJ, 145, 10
Denney, K. D., De Rosa, G., Croxall, K., et al. 2014, ApJ, 796, 134
Dexter, J., & Begelman, M. C. 2019, MNRAS, 483, L17
Doré, O., Werner, M. W., Ashby, M. L. N., et al. 2018, arXiv:1805.05489
Drake, A. J., Djorgovski, S. G., Graham, M. J., et al. 2019, MNRAS, 482, 98
Drake, A. J., Djorgovski, S. G., Mahabal, A., et al. 2009, ApJ, 696, 870
Eisenstein, D. J., Weinberg, D. H., Agol, E., et al. 2011, AJ, 142, 72
Elitzur, M., & Ho, L. C. 2009, ApJL, 701, L91
Elitzur, M., Ho, L. C., & Trump, J. R. 2014, MNRAS, 438, 3340
Eracleous, M., & Halpern, J. P. 2001, ApJ, 554, 240
Evans, I. N., Allen, C. E., Anderson, C. S., et al. 2018, AAS Meeting, 231, 238.01
Fausnaugh, M. M., Denney, K. D., Barth, A. J., et al. 2016, ApJ, 821, 56
Flewelling, H. A., Magnier, E. A., Chambers, K. C., et al. 2016, arXiv:1612.05243
Fukugita, M., Ichikawa, T., Gunn, J. E., et al. 1996, AJ, 111, 1748
Gezari, S., Hung, T., Cenko, S. B., et al. 2017, ApJ, 835, 144
Goodrich, R. W. 1989, ApJ, 340, 190
Goodrich, R. W. 1990, ApJ, 355, 88
Graham, M. J., Djorgovski, S. G., Drake, A. J., et al. 2017, MNRAS, 470, 4112
Graham, M. J., Kulkarni, S. R., Bellm, E. C., et al. 2019, arXiv:1902.01945
Guillochon, J., Manukian, H., & Ramirez-Ruiz, E. 2014, ApJ, 783, 23
Gunn, J. E., Carr, M., Rockosi, C., et al. 1998, AJ, 116, 3040
Gunn, J. E., Siegmund, W. A., Mannery, E. J., et al. 2006, AJ, 131, 2332
Hogg, D. W., Finkbeiner, D. P., Schlegel, D. J., & Gunn, J. E. 2001, AJ, 122, 2129
Husemann, B., Urrutia, T., Tremblay, G. R., et al. 2016, A&A, 593, L9
Inserra, C., Smartt, S. J., Jerkstrand, A., et al. 2013, ApJ, 770, 128
Ivezić, Ž., Lupton, R. H., Schlegel, D., et al. 2004, AN, 325, 583
Ivezic, Z., Tyson, J. A., Abel, B., et al. 2008, arXiv:0805.2366
Jiang, Y.-F., Davis, S. W., & Stone, J. M. 2016, ApJ, 827, 10
Kaiser, N., Aussel, H., Burke, B. E., et al. 2002, Proc. SPIE, 4836, 154

Khachikian, E. Y., & Weedman, D. W. 1971, ApJL, 164, L109
Kim, D.-W., Protopapas, P., Byun, Y.-I., et al. 2011, ApJ, 735, 68
Kimball, A. E., & Ivezić, Ž. 2014, in IAU Symp. 304, Multiwavelength AGN Surveys and Studies, ed. A. M. Mickaelian & D. B. Sanders (Cambridge: Cambridge Univ. Press), 238
Kollatschny, W., & Bischoff, K. 2002, A&A, 386, L19
Kollmeier, J. A., Zasowski, G., Rix, H.-W., et al. 2017, arXiv:1711.03234
Korista, K. T., & Goad, M. R. 2004, ApJ, 606, 749
Kozłowski, S., Kochanek, C. S., Udalski, A., et al. 2010, ApJ, 708, 927
Krolik, J. H. 1999, Active Galactic Nuclei: from the Central Black Hole to the Galactic Environment (Princeton, NJ: Princeton Univ. Press)
Kubota, A., & Done, C. 2018, MNRAS, 480, 1247
LaMassa, S. M., Cales, S., Moran, E. C., et al. 2015, ApJ, 800, 144
Lawrence, A. 2012, MNRAS, 423, 451
Lawrence, A. 2016, in ASP Conf. Ser. 505, Astronomical Surveys and Big Data, ed. A. Mickaelian, A. Lawrence, & T. Magakian (San Francisco, CA: ASP), 107
Li, Y., Yuan, W., Zhou, H. Y., et al. 2015, AJ, 149, 75
Liu, T., Merloni, A., Wang, J.-X., et al. 2018, MNRAS, 479, 5022
LSST Science Collaboration, Abell, P. A., Allison, J., et al. 2009, arXiv:0912.0201
Lupton, R., Gunn, J. E., Ivezić, Z., Knapp, G. R., & Kent, S. 2001, in ASP Conf. Ser. 238, Astronomical Data Analysis Software and Systems X, ed. F. R. Harnden, Jr., F. A. Primini, & H. E. Payne (San Francisco, CA: ASP), 269
MacLeod, C. L., Green, P. J., Anderson, S. F., et al. 2018, AJ, 155, 6
MacLeod, C. L., Ivezić, Ž., Kochanek, C. S., et al. 2010, ApJ, 721, 1014
MacLeod, C. L., Ross, N. P., Lawrence, A., et al. 2016, MNRAS, 457, 389
Magnier, E. A., Chambers, K. C., Flewelling, H. A., et al. 2016a, arXiv:1612.05240
Magnier, E. A., Schlafly, E. F., Finkbeiner, D. P., et al. 2016b, arXiv:1612.05242
Magnier, E. A., Sweeney, W. E., Chambers, K. C., et al. 2016c, arXiv:1612.05244
Merloni, A., Dwelly, T., Salvato, M., et al. 2015, MNRAS, 452, 69
Morganson, E., Green, P. J., Anderson, S. F., et al. 2015, ApJ, 806, 244
Nicastro, F. 2000, ApJL, 530, L65
Nixon, C., King, A., Price, D., & Frank, J. 2012, ApJL, 757, L24
Noda, H., & Done, C. 2018, MNRAS, 480, 3893
Osterbrock, D. E. 1981, ApJ, 249, 462
Osterbrock, D. E., Shaw, R. A., & Veilleux, S. 1990, ApJ, 352, 561
Padmanabhan, N., Schlegel, D. J., Finkbeiner, D. P., et al. 2008, ApJ, 674, 1217
Penston, M. V., & Perez, E. 1984, MNRAS, 211, 33P
Peterson, B. M., Ferrarese, L., Gilbert, K. M., et al. 2004, ApJ, 613, 682
Pier, J. R., Munn, J. A., Hindsley, R. B., et al. 2003, AJ, 125, 1559
Polletta, M., Tajer, M., Maraschi, L., et al. 2007, ApJ, 663, 81
Quimby, R. M., Oguri, M., More, A., et al. 2014, Sci, 344, 396
Richards, G. T., Fan, X., Newberg, H. J., et al. 2002, AJ, 123, 2945
Richards, G. T., Kruczek, N. E., Gallagher, S. C., et al. 2011, AJ, 141, 167
Risaliti, G., Miniutti, G., Elvis, M., et al. 2009, ApJ, 696, 160
Rosen, S. R., Webb, N. A., Watson, M. G., et al. 2016, A&A, 590, A1
Ross, N. P., Ford, K. E. S., Graham, M., et al. 2018, MNRAS, 480, 4468
Ruan, J. J., Anderson, S. F., Cales, S. L., et al. 2016, ApJ, 826, 188
Rumbaugh, N., Shen, Y., Morganson, E., et al. 2018, ApJ, 854, 160
Runco, J. N., Cosens, M., Bennert, V. N., et al. 2016, ApJ, 821, 33
Runnoe, J. C., Cales, S., Ruan, J. J., et al. 2016, MNRAS, 455, 1691
Runnoe, J. C., Eracleous, M., Pennell, A., et al. 2017, MNRAS, 468, 1683
Schneider, D. P., Richards, G. T., Hall, P. B., et al. 2010, AJ, 139, 2360
Shakura, N. I., & Sunyaev, R. A. 1973, A&A, 24, 337
Shappee, B. J., Prieto, J. L., Grupe, D., et al. 2014, ApJ, 788, 48
Shen, Y., Horne, K., Grier, C. J., et al. 2016, ApJ, 818, 30
Shen, Y., Richards, G. T., Strauss, M. A., et al. 2011, ApJS, 194, 45
Silva, L., Granato, G. L., Bressan, A., & Danese, L. 1998, ApJ, 509, 103
Smith, J. A., Tucker, D. L., Kent, S., et al. 2002, AJ, 123, 2121
Stern, D., Graham, M. J., Arav, N., et al. 2017, ApJ, 839, 106
Stern, D., McKernan, B., Graham, M. J., et al. 2018, ApJ, 864, 27
Storchi-Bergmann, T., Baldwin, J. A., & Wilson, A. S. 1993, ApJL, 410, L11
Stoughton, C., Lupton, R. H., Bernardi, M., et al. 2002, AJ, 123, 485
Strateva, I. V., Strauss, M. A., Hao, L., et al. 2003, AJ, 126, 1720
Tohline, J. E., & Osterbrock, D. E. 1976, ApJL, 210, L117
Tucker, D. L., Kent, S., Richmond, M. W., et al. 2006, AN, 327, 821
Véron-Cetty, M.-P., Joly, M., & Véron, P. 2004, A&A, 417, 515
Vestergaard, M., & Wilkes, B. J. 2001, ApJS, 134, 1
Wade, R. A., & Horne, K. 1988, ApJ, 324, 411
Wang, J., Xu, D. W., & Wei, J. Y. 2018, ApJ, 858, 49
Waters, C. Z., Magnier, E. A., Price, P. A., et al. 2016, arXiv:1612.05245
Wilhite, B. C., Brunner, R. J., Grier, C. J., Schneider, D. P., & vanden Berk, D. E. 2008, MNRAS, 383, 1232
Yang, Q., Wu, X.-B., Fan, X., et al. 2018, ApJ, 862, 109
York, D. G., Adelman, J., Anderson, J. E., Jr., et al. 2000, AJ, 120, 1579